VNIVERSITY OF SALAMANCA

FACVLTY OF SCIENCE

DEPARTMENT OF APPLIED PHYSICS

GaN nanodevices for THz signal generation. Monte Carlo simulation and experimental analysis

SVMMARY OF THE DOCTORAL THESIS

Ana Íñiguez de la Torre Mulas

Salamanca, 2012

Dr. Tomás González Sánchez, Full Professor of Electronics in the Department of Applied Physics at the University of Salamanca,

CERTIFIES that:

The research work collected in this summary, entitled *GaN nanodevices for THz signal generation. Monte Carlo simulation and experimental analysis*, presented by **Ana Íñiguez de la Torre Mulas** to apply for the PhD degree, has been carried out under his direction at the Electronics Group in the Department of Applied Physics at the University of Salamanca.

Salamanca, November, 12nd 2012

Tomás González Sánchez
Full Professor of Electronics
Department of Applied Physics
University of Salamanca

TABLE OF CONTENTS

INTRODUCTION **1**

I. MONTE CARLO MODEL: METHODOLOGY **9**

I.1. Generalities of a single particle simulator 9

I.2. Device Monte Carlo simulator 10

I.3. GaN, from the semiconductor to the device 11

I.4. Spectral density of current fluctuations and DC to AC efficiency 15

II. CURRENT OSCILLATIONS ASSISTED BY OPTICAL PHONON EMISSION IN GaN n^+nn^+ DIODES **17**

II.1. OPTTR: concept and conditions 18

II.1.a. Single particle 18

II.1.b. Collective phenomenon 19

II.2. Monte Carlo simulations and results 20

II.2.a. OPTTR in bulk GaN 20

II.2.b. n^+nn^+ diodes: reference structure 22

II.2.c. n^+nn^+ diodes: temperature influence 25

II.2.d. n^+nn^+ diodes: length influence 26

II.2.e. n^+nn^+ diodes: doping influence 27

III. GUNN OSCILLATIONS IN GaN SSDs 29

III.1. Literature review: SSDs and Gunn effect 30

III.1.a. Overview of the SSD 30

III.1.b. The Gunn effect 33

III.2. Preliminary simulations with the constant surface charge model 34

III.2.a. Influence of the model parameters (σ and N_{Db}) 35

III.2.b. Influence of the temperature and geometric parameters 36

III.2.c. Study of the efficiency 37

III.2.d. Evolution of microscopic quantities 39

III.3. Comparison with experimental results of Run 1 40

III.3.a. First experimental measurements 40

III.3.b. Comparison with the constant surface charge model 42

III.3.c. Comparison with the self-consistent surface charge model 43

III.3.d. Study of several quantities 45

III.4. New design strategies and fabrication of Run 2 47

III.4.a. Indications with the constant surface charge model 47

III.4.b. Indications with the self-consistent surface charge model 47

III.4.c. Experimental measurements 49

III.5. Simulations and experimental measurements in Run 3 51

III.5.a. Design and fabrication 51

III.5.b. Simulations and experimental measurements 52

IV. CORRELATION BETWEEN LOW-FREQUENCY NOISE AND HIGH-FREQUENCY OSCILLATIONS 55

IV.1. Low frequency noise in SSDs 56

IV.2. Low frequency noise in the OPTTR 59

CONCLUSIONS 61

REFERENCES 69

INTRODUCTION

Since the experimental verification of electromagnetic radiation and propagation in 1888 by the German physicist Heinrich Rudolf Hertz,[1] the several frequency bands in the electromagnetic spectrum are more and more exploited to very different purposes.

A. The THz gap

However, there is a frequency interval around terahertz (THz≡10^{12} Hz) frequencies in which a lot of work is still to be done in order to achieve sources, amplifiers and detectors of signals. In fact, the frequencies between approximately 100 GHz and 10 THz (what is equivalent to wave lengths between 3 mm and 30 µm) are typically referred as the terahertz gap, and, as observed in Figure 1, they are placed just between the regions exploited by electronics and photonics.

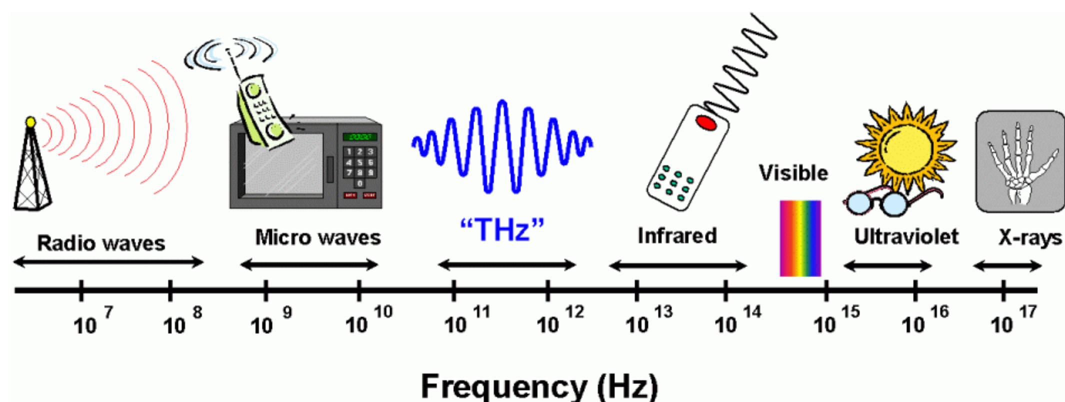

Figure 1. Location of the so called terahertz gap within the electromagnetic spectrum. *Image* extracted from: http://www.sp.phy.cam.ac.uk/SPWeb/research/thzcamera/WhatIsTHzImaging.htm.

Such a band in the spectrum constitutes a substantial fraction of the residual radiation of the Big Bang due to the red displacement lying in the THz domain, where the radiation from the temperature of biological processes also lies.[2]

B. Applications

Nowadays, the THz frequency band is considered of great interest because of its potential application in manifold fields like physics, astronomy, chemistry, biology, medical diagnosis, spectroscopy, tomography, environmental control, biological and chemical identification, etc.[2-13]

THz radiation hardly interacts with certain apolar molecules (paper, cloths, wood, ethylene, CO_2, etc.), while it does interact with polar molecules (water, ammonia, etc.) and with free carriers of metal or doped semiconductors; such that it can penetrate organisms, but, in contrast to X-rays, it is not ionizing, what evidently constitutes a key aspect at the time of being used with human beings. We must note that penetration and absorption of the so called T-rays depend on the material and operation frequency. For example, at a few THz the penetration depth through water solutions is very limited, while plastic substances are essentially transparent. As a consequence, if tunable sources and detectors of THz radiation were available, nearly any object could be easily scanned. This is giving rise to new initiatives in medicine, in the battle against cancer and other diseases, which could be detected in earlier stages. Likewise, fight against terrorism would meet an exceptional ally in this radiofrequency tool. With the aim of illustrating some of these applications, we show in Figure 2 and Figure 3 several images belonging to *TeraView* and *ThruVision*, two leading companies in THz commercial applications.

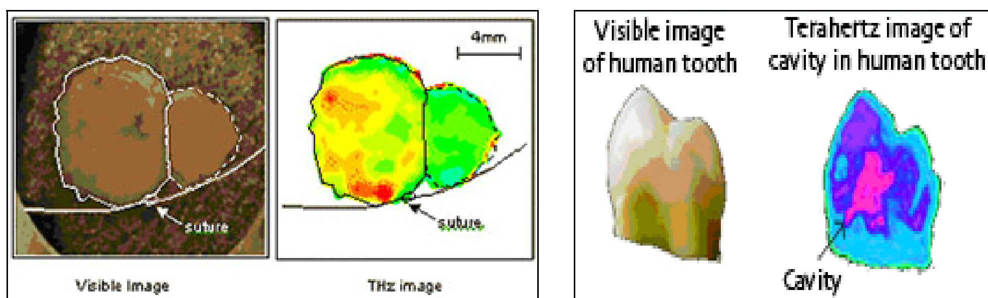

Figure 2. THz technology for skin cancer detection and dental health.

Figure 3. THz technology of weapons and explosives detection.

C. Last progresses in detection and emission

The THz gap is difficult to be filled from the point of view of both detection and emission. Let us mention some of the most relevant technologies that emerge as promising candidates to conquer this frequency interval. In Refs. 14 and 15, abundant information about this and other techniques is collected.

As concerns THz detection we underline three approaches. The first one is thermal detectors, as bolometers, Golay cells or piroelectrics. The second one is electronic devices as Schottky detectors (mainly operating as heterodyne receptors), or field effect transistors exploiting plasma oscillations in a two-dimensional electron gas. Finally, the third one is detectors based on quantum phenomena, as photodetectors and systems using electro-optical sampling. In all of them, the figures of merit allowing quantifying their performance are responsivity, noise equivalent power and response time.

Three are the main possibilities for signal generation. The first one is the optical approach, where the main tools are quantum cascade lasers (QCLs)[16] and the use of non-linear optical materials to decrease the frequency of the typical sources in this band. Another option, in principle quite adequate in terms of power and frequency, is the germanium laser, but it has the disadvantage of cryogenic and pulse operation. The second alternative is the electronic approach,[17] the most promising devices being frequency multipliers based on Schottky barrier diodes (SBDs), which, as sources of lower-frequency signals, use resonant-tunneling diodes (RTDs), Gunn diodes and IMPATT (IMPact ionization Avalanche Transit Time) diodes, and oscillators based on both HBTs (Heterojunction Bipolar Transitors) and HEMTs (High-Electron Mobility Transistors). The last approach is related to optoelectronics, in which the most common systems used to this end, even if they are quite bulky, are

photomixers and electro-optical systems, mainly used in spectroscopy and based on the excitation of semiconductors with fs lasers. Figure 4 shows the emitted power as a function of frequency for the main candidates as emitters in the THz range.

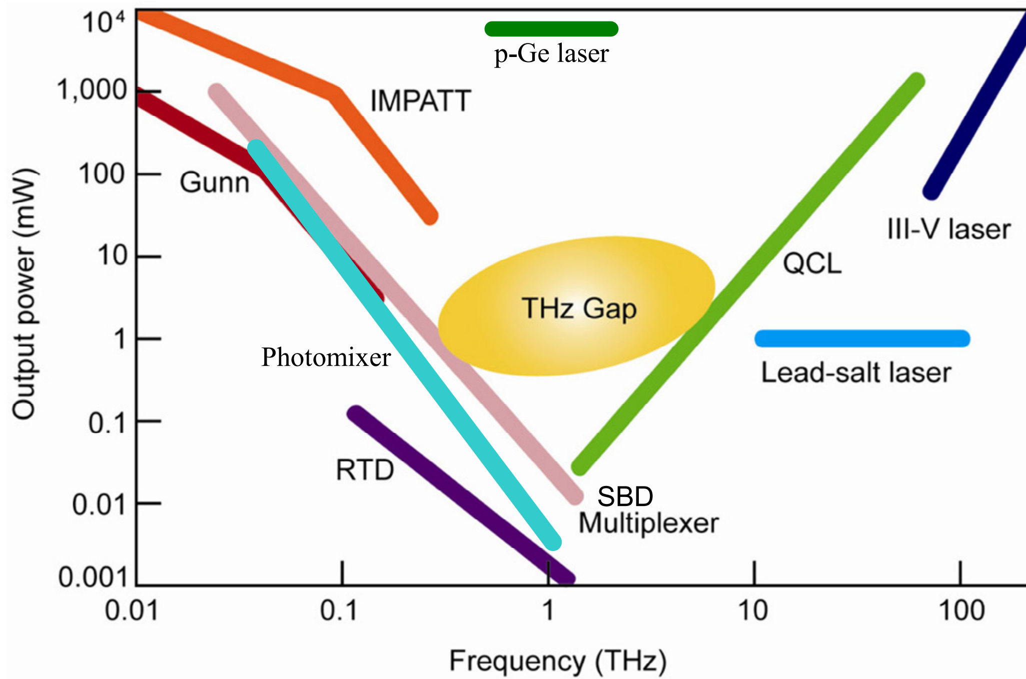

Figure 4. State-of-the-art in emission sources at frequencies around terahertz.

Despite of the great expectation placed on the progress of THz technology, currently only some elemental sources of very low power have been achieved. Such limited advancement of research in this field is due to two factors. Firstly, with particular regard to the electronic approach, the great engineering challenge which represents the fabrication of very small devices, comparable in size to v/f, being v the electron velocity in the material and f the operation frequency. And secondly, the limited demand of these devices till ten years ago, since their applications were restricted nearly exclusively to so specialized fields like molecular spectroscopy and radioastronomy. However, with the new millennium important applications of THz signals have emerged, as previously mentioned, in fields like defense, telecommunications, identification of chemical composites and biological substances, etc.

D. The solution from solid-state electronics

Electronic transport processes determine the basic principles of operation of most semiconductor devices and, what is more, they establish the relevant device properties of nearly all devices of interest in high-speed electronics. Thus, advanced

techniques for the study of the physical processes involved in high-speed carrier dynamics play a crucial role in the progress of high-frequency electronics. For example, improvements in solid-state devices using electronic-transport control and velocity modulation have had a fundamental impact in microwave technology.[18] The inventions of the transistor by Shockley, the bipolar junction transistor (BJT) and field-effect transistors (FET and MOSFET) definitively revolutionized high-speed electronics. Of course, it was the result of the advantages in functionality, miniaturization and low cost of solid-state devices as compared to the previous devices based on vacuum-tubes for low-power applications. However, conventional semiconductor devices present performance limitations at sub-millimeter waves. Thus, new semiconductor devices must be designed to become the basis for generation, amplification and detection of millimeter and sub-millimeter signals. Despite the recent efforts in this line, nowadays the frequency band between microwave and infrared radiation still constitutes a technological challenge.

Nanotechnology is currently pushing the development of THz devices. The progress towards nanoelectronics and molecular electronics seems to suggest completely new device technologies (like, for example, spin electronics),[19] the study of which requires a rigorous quantum treatment. On the other hand, the nanometric dimensions of novel devices involve the appearance of new problems to face: ballistic transport, non-equilibrium processes, dissipative scattering, etc., which require a great level of knowledge of solid-state physics.[20]

As previously mentioned, in the field of electronics several alternatives can be found in order to develop efficient emitters and detectors in the THz range: Gunn diodes, frequency multipliers, Schottky detectors, plasma oscillations devices, etc.

E. Objectives and outline of the PhD thesis

It is in this point where this work intends to make a contribution by means of the analysis of two candidates from the approach based on solid-state devices (see Figure 5), mainly oriented to the generation of signals of such high frequency, exploiting (i) coherent plasma oscillations in micrometric diodes induced by optical phonon emission (OPTTR, Optical Phonon Transit Time Resonance)[21-23] and (ii) Gunn oscillations[24-26] in nanometric Self-Switching Diodes (SSDs).[27]

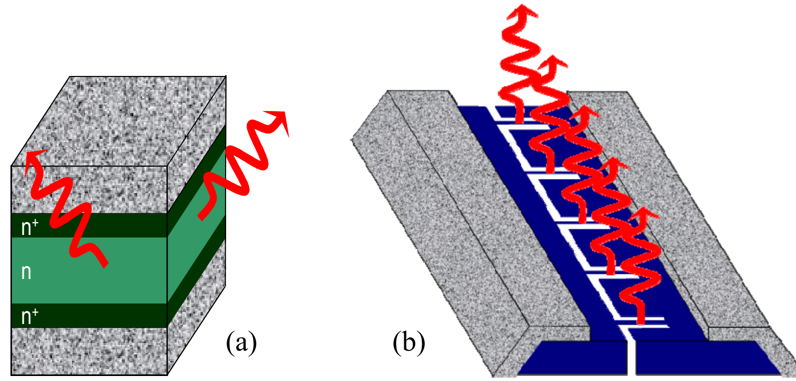

Figure 5. Mechanisms and devices analyzed in this work for the generation of THz signals: (a) OPTTR in n^+nn^+ diodes and (b) Gunn oscillations in SSDs.

In both cases gallium nitride (GaN) has been chosen as the material on which devices are based. As we will show later in this thesis, among other characteristics, this wide band-gap material is considered as a very good candidate for high-frequency and high-power applications because of its saturation electron velocity, threshold and breakdown electric fields, higher than in conventional semiconductors; the latter field being a key feature to support extremely high DC bias.[28] In the case of the OPTTR, the selection of GaN is due to the high value of the polar phonon energy in this material, which, as we will show, is a key factor when trying to obtain significant current oscillations.

The ability of these two devices to operate at extremely high frequency comes from instability/oscillation processes that take place, under certain conditions and/or particular geometries, as a consequence of interactions at micrometric and nanometric scale. These interactions must be studied in detail to achieve the optimization of the device operation, such that the processes generating the oscillations are not cancelled by other effects.[29]

OPTTR is a phenomenon taking place under some specific conditions in electronic devices that can give rise to current oscillations of very high frequencies, reaching even THz values. It consists in the oscillations induced by optical phonon emission, coupled in quasi-ballistic regime to the plasma frequency of the active region of a semiconductor diode. In a resumed way, the idea is to take advantage of the periodic carrier dynamics originated by optical phonon emission when a constant voltage is applied to the device. The carriers, accelerated by the electric field, move ballistically till gaining the energy corresponding to an optical phonon, that they immediately emit, and then repeat the acceleration/emission cycle. This cyclic

sequence of carrier acceleration and breaking leads to charge accumulations in some localized regions of the device (charge-density modulation) which, under certain conditions, will originate high-frequency oscillations in the current flowing through the diodes.

As a second approach, the search for high-frequency oscillation in SSDs is based on Gunn effect. As a consequence of electron transfer to upper valleys, where electrons behave with a higher effective mass, charge domains are formed (under some conditions), which travel along the channels, leading to current oscillations. SSDs are in principle relatively easy to fabricate, since they are planar structures with the symmetry broken by the etching of L-shaped isolating trenches that define the channel. In our research group, we started studying these devices several years ago, and nowadays, within the framework of the European Project *ROOTHz* (Semiconductor Nanodevices for Room Temperature THz Emission and Detection) that we coordinate, we continue working on them with the ambitious objective, among others, of achieving the generation of THz signals at room temperature.

Research in these fields requires both simulation and experiments. Device fabrication and characterization are extraordinarily complex and expensive, so that the previous simulation of the structures becomes essential in their correct design. The efforts on both sides are complementary and result in save of time and cost. In particular, our work is mainly based on the Monte Carlo (MC) method,[30-32] a simulation technique with significant advantages over other ones, since it includes in a direct way the microscopic random processes taking place in electron transport, which results to be of great importance in high-frequency phenomena.

According to all what explained previously, this memory is organized in four chapters. In the first chapter we explain the tool used in the calculations, a MC simulator. Both the techniques used to study the material properties and those employed to analyze the complete devices will be described. We will present the most relevant properties of GaN, mainly those related to THz signal generation. Finally we will explain the process followed for the calculation and treatment of some of the simulation results.

Next, in the second chapter, after a brief summary of plasma physics in solids, the theoretical fundamentals of OPTTR are explained. Some pioneering results from other authors are initially shown, but we must remark that this is a field scarcely

explored, and the few literature on the subject refers to other nitrides rather than GaN. We will show and analyze our results, obtained both with a single particle simulator for bulk GaN and then already on GaN n^+nn^+ diodes. In the latter case we start with a reference structure, on which several parameters are modified in order to study their influence on the phenomenon under analysis, concretely paying special attention on the effect of temperature, doping and length of the diode active region. Collecting all this information, the optimum design of the diodes for the exploitation of the phenomenon is tentatively proposed.

The third chapter deals with SSDs. Analogously to the previous chapter, we start explaining the physical phenomenon involved in this case, the Gunn effect. Then the device under analysis is presented, its main characteristics and the technological processes followed for its fabrication. Simulation results obtained with the different models used are shown afterwards. Since, as we explained, simulation and fabrication processes have gone hand in hand, with one progressing with the results from the other and vice versa, the results will be presented chronologically, both those obtained with our simulations and the comparison with experiments, some of them performed by myself during a three-month stay at the IEMN (*Institut d'Electronique, de Microélectronique et de Nanotechnologie*) in Lille (France). In this way, the different steps followed in the design of the several fabrication runs that have been carried out will be more easily understood. Even if the final aim of the European project is to achieve a compact THz detection/emission system working at room temperature, my personal contribution has been mainly focused on the emission topic. Nevertheless, an appendix (not reported in this summary) explaining the main detection results is enclosed in order to complete this work.

The fourth chapter presents an analysis about the link existing between the increase of low-frequency current noise in the devices and the onset of the THz oscillations that our simulations show in both analyzed mechanisms. Due to the inherent difficulties existing when trying to experimentally detect the presence of oscillations in the THz (and even sub-THz) band, the measurement of low-frequency noise can be a very useful tool for indirect detection of their presence, according to what simulations predict.

We will finish the PhD dissertation with the main conclusions extracted from our work.

I. MONTE CARLO MODEL: METHODOLOGY

In this chapter, a general overview of how our home-made Monte Carlo (MC) simulator operates is provided. A more detailed explanation can be found in the several doctoral theses carried out in our group along the last twenty years.[33-39] Since the development of the method,[40-42] applied for the first time to semiconductor simulations in 1966,[43-44] it has been established as the most detailed technique to simulate electronic devices as compared to other ones like drift-diffusion[45] or hydrodynamic models.[46]

I.1. Generalities of a single particle simulator

The single particle simulator is used to study the properties of bulk semiconductors under the action of a constant electric field (steady-state, homogeneous conditions). It consists of simulating the motion of a charged carrier inside the crystal making use of random numbers to manage the different statistical distributions involved in the process. It is intended to study the free flights of the particle accelerated by an applied electric field between instantaneous random scattering events. In more detail [Figure 6(a)], the algorithm generates random free flight times, determines the electron state at the end of the free flight and randomly chooses the scattering mechanism taking place from amongst those possible, computes the final energy and momentum of the particle after scattering, and finally reiterates the routine for the subsequent free flight. By monitoring the particle motion during the simulation, it is possible to statistically estimate the value of several physical quantities such as the distribution function, average drift velocity, average energy, etc.

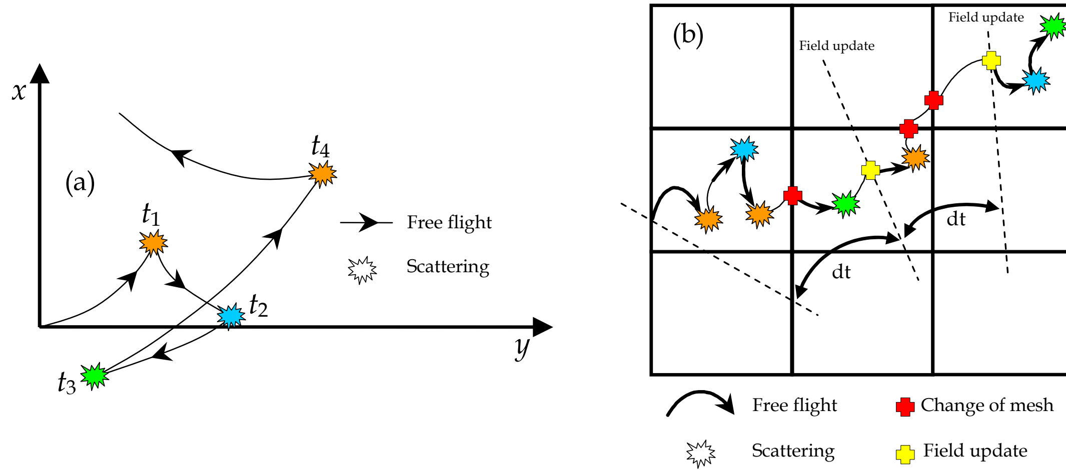

Figure 6. (a) Simple diagram of the particle motion in the real space under a uniform electric field applied in the x direction. (b) 2D device simulator scheme.

I.2. Device Monte Carlo simulator

When non-stationary (but still homogeneous) conditions are studied, a synchronous simulation of a reasonable number of particles is necessary. This is called ensemble MC, in which the above algorithm is repeated for each particle. Every given time step dt, during which the individual carriers are simulated independently, the quantities of interest are sampled and averaged to obtain the (time-dependent) information of interest.

In the case of a real semiconductor device (non-homogeneous and finite system), it is additionally essential to consider the correct spatial distribution of the electric potential, achieved by means of a solver of Poisson's Equation (PE). Consequently, it becomes necessary to couple the transport kernel and the field solver to each other. For this purpose a spatial grid, being the mesh size smaller than the Debye length, is needed to solve the PE.[30] In this frame the simulation of the particle-based ensemble is carried out over a reasonably small time step, under the action of a self-consistent electric field (solution of PE at the end of the previous iteration) with appropriate boundary conditions.[47] At the end of each time interval, PE for the next time-step is solved again using the configuration of charges obtained from the MC ensemble [Figure 6(b)].

The electric field is computed (neglecting the inductive magnetic effects) from the solution of PE achieved by LU[48] decomposition of the linear system of equations resulting from a finite differences approach. Accurate scattering probabilities for

ionized impurity, alloy, polar and non-polar optical phonon, acoustic phonon and intervalley scattering are used within a non-parabolic spherical band-structure model. We have to remark that the carrier-carrier scattering in not included.[49,50] The energy dependence of the probability of each scattering mechanism and the final state after the interaction can be looked up in the references.[51-54] Neumann boundary conditions (the difference between the normal components of the respective electric displacement vectors must be equal to any surface charge) are imposed at the semiconductor/dielectric boundaries, so that current only flows in/out of the device through the contacts, in which a Dirichlet condition (the potential is fixed) is imposed. The value of the time step, dt, has also to fulfill some restrictions. It is limited by the inverse of the plasma frequency[55] f_p and by the dielectric relaxation time[56] τ_d, in such a way that $2\pi f_p dt < 2$ and $dt < \tau_d$.

I.3. GaN, from the semiconductor to the device

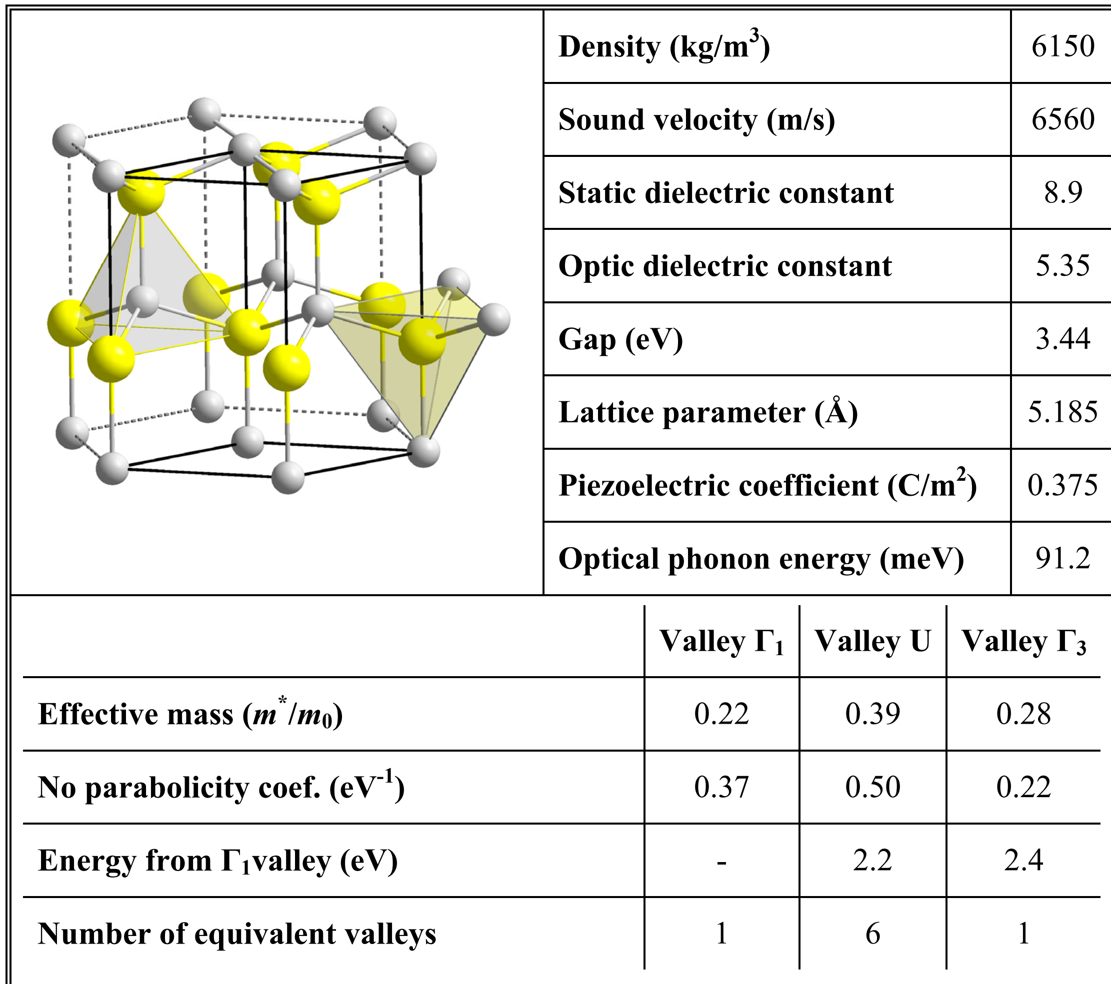

Density (kg/m^3)	6150
Sound velocity (m/s)	6560
Static dielectric constant	8.9
Optic dielectric constant	5.35
Gap (eV)	3.44
Lattice parameter (Å)	5.185
Piezoelectric coefficient (C/m^2)	0.375
Optical phonon energy (meV)	91.2

	Valley Γ_1	**Valley U**	**Valley Γ_3**
Effective mass (m^*/m_0)	0.22	0.39	0.28
No parabolicity coef. (eV^{-1})	0.37	0.50	0.22
Energy from $\Gamma_1$valley (eV)	-	2.2	2.4
Number of equivalent valleys	1	6	1

Table 1. Material parameters for bulk GaN

Initially, the single particle simulator is used to calibrate the model and fix the values of the material parameters of bulk GaN from those found in the literature (exhibiting great dispersion)[57-59] by fitting experimental mobility and velocity-field characteristics.[60,61] Table 1 collects the main parameters used in our MC simulator for gallium nitride with wurtzite crystal structure (α-GaN), the material on which our devices are based. The conduction band is modeled by three non-parabolic spherical valleys (Γ_1, U and Γ_3). Other relevant parameters at room temperature are: breakdown electric field of 3.3 MV/cm and thermal conductivity of 2.1 W/cmK.[62] Typical values of electron mobility and saturation velocity achieved with our model are around 900 cm^2/Vs and 1.5×10^7 cm/s, respectively, in good agreement with experimental values.

Once the material is correctly modeled, we make use of the semiclassical ensemble MC simulator self-consistently coupled with a 2D Poisson solver to study two different devices: n^+nn^+ diodes and Self-Switching Diodes (SSDs). The transport model locally takes into account the effect of degeneracy and electron heating by using the rejection technique and the self-consistent calculation of the local electronic temperature and Fermi level. The surface charges appearing at the boundaries of the semiconductors in contact with dielectrics are also considered in the model. The validity of this approach has been checked in previous works by means of the comparison with experimental results of static characteristics, small signal behavior and noise performance of HEMTs based on different types of heterostructures like AlInAs/GaInAs,[63] AlGaN/GaN,[64-66] AlInSb/InSb[67] or InAs/AlSb.[68]

The simulation of the n^+nn^+ diodes follows the standard scheme and involves no special complications (no surface charges are considered) thanks to their transversal symmetry. Indeed, even if we use a 2D simulator for their analysis, they are essentially 1D devices.

That is not the case of SSDs. As the SSD is intrinsically a 3D device [Figure 7(a)], for its correct modeling a 3D simulation would be necessary. However, for the moment, only a 2D MC model has been developed, and some simplifications and assumptions must be made. So, as shown in Figure 7(b), where the shape of the simulation domain (which includes access regions) is sketched, only the GaN layer is considered in the so-called “top-view” simulations, where we include two ad hoc

parameters: (i) a "virtual" background net doping, N_{Db}, is assigned to this layer (although the associated scattering is not considered) in order to account for the fixed charges at the top surface and the heterojunction, and (ii) a negative surface charge density, σ, is assigned to the semiconductor-air interfaces to account for the influence of the surface states originated during the etching process. N_{Db} and σ are the only two parameters of our MC model to be fixed by comparison between simulations an experimental data. In addition, our approach has recently been further validated by the results of Ref. 69 whose results using a 3D model have been almost perfectly replicated with our 2D model for the same set of devices.

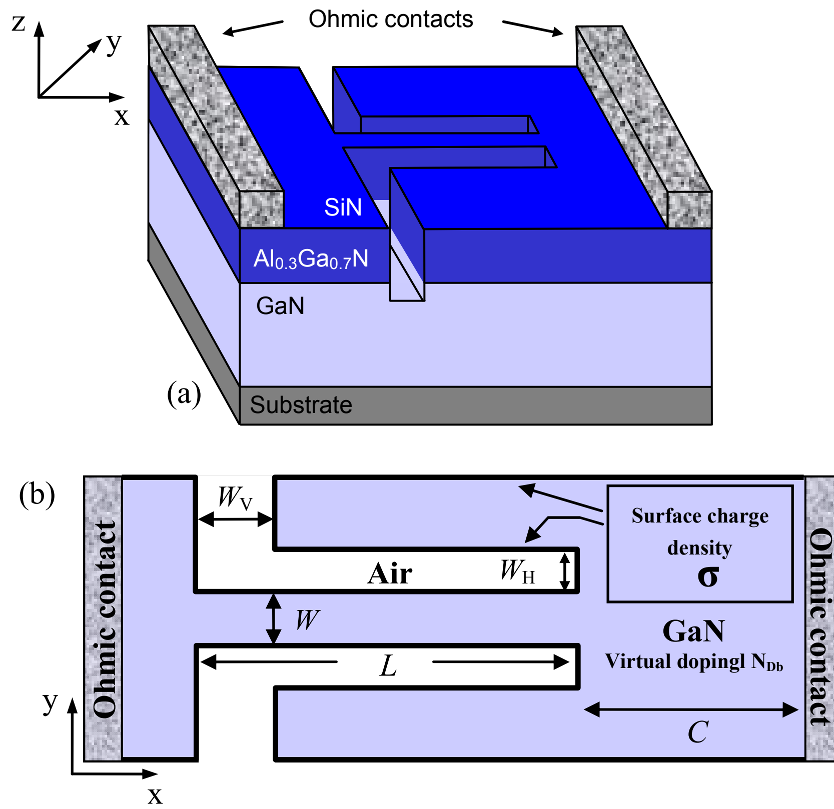

Figure 7. (a) Typical geometry of SSDs and (b) scheme of the top-view simulations of the GaN channel with the involved parameters ("virtual" doping N_{Db} and negative surface charge density σ). L and W are the length and width of the channel respectively, W_H the width of the horizontal trenches, W_V the width of the vertical ones and C the length of the anode access region.

The negative value of the surface charge σ (associated with electrons trapped at surface states) leads to a depletion of the channel near the sidewalls as a consequence of Coulomb repulsion. The depletion width at each side of the channel can be estimated as $W_d = \sigma / N_{Db}$. Therefore, the effective conduction width is $W_{eff} = W - 2W_d$ [Figure 8(a)], with W the lithographic width of the channel.

Typically, with the aim of extracting the experimental lateral depletion width W_d, the electrical characterization of channels with different length and width has been made. The simplest and more standard model for including σ, is to give it a constant value independently of the topology, bias and time (constant surface charge model). But in order to correctly simulate the global effect of surface charges on the electron transport in nanodevices a self-consistent surface charge model should be used.[38] In such an improved model the local value of the surface charge is continuously updated according to the value of the carrier density nearby until a stationary behavior is achieved.

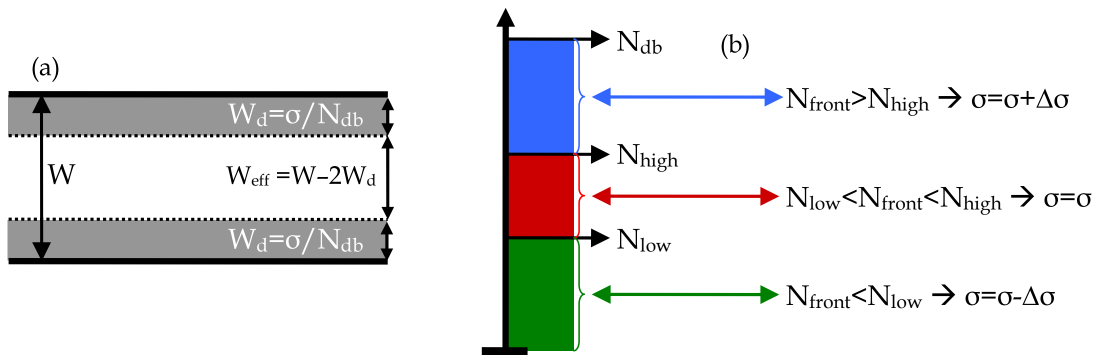

Figure 8. (a) Effective channel width due to lateral depletion. (b) Surface charge adjustment in the self-consistent model.

The philosophy of the model is explained as follows [Figure 8(b)]. First, the carrier concentration next to the boundary (N_{front}) is evaluated as an average over a given number of iterations N_{i}. Then, it is checked if N_{front} has a value in the range [N_{low}, N_{high}]. If the concentration (N_{front}) is higher than the upper limit (N_{high}), the surface charge is increased in a given amount Δσ, so that its repulsive effect provokes stronger channel depletion and thus the concentration should diminish. On the other hand if N_{front} is smaller than the lower limit (N_{low}), the surface charge is decreased in the same density $\Delta\sigma$ to reduce the (too large) induced depletion. It is important to remark that evidently this ad hoc surface charge model is not able to reproduce the statistics of occupation of surface states, but it does describe correctly the global effect of the surface charge. Our group has successfully applied this self-consistent model to explain the working principle of several ballistic nanodevices like four terminal ballistic rectifiers,[70] three-terminal ballistic junctions (TBJs and YBJs),[71-73] ballistic deflection transistors (BDTs)[74] and even SSDs[75], all based on InAlAs/InGaAs layers; the comparison of the results with experimental

measurements providing a very satisfactory agreement.[76] The calculations in this thesis will make use of this model in GaN diodes for the first time.

I.4. Spectral density of current fluctuations and DC to AC efficiency

The instantaneous values of the current are calculated using the generalized Ramo-Shockley theorem,[77,78] which evaluates the simultaneous contribution of all super particles involved in the MC simulation to the total electrode current.[79-84]

For the analysis of the current sequences in the frequency domain we use the Fast Fourier Transform (FFT) procedure to calculate the spectral density $S_I(f)$. In particular, we use the method described in the Ref. 48. The typically number of samples employed is 2^{19} of a total of 600.000 simulated iterations (300 ps with $dt = 0.5$ fs), so that the frequency resolution is quite precise, of around $\Delta f \approx 3$ GHz.[85]

The DC to AC conversion efficiency is evaluated in order to analyze the SSDs performance as emitters. To this end, we used a common technique already used by other authors [Refs. 86-88]: a single-tone sinusoidal potential of amplitude V_{AC} is superimposed to a DC bias V_{DC}. These working conditions are somehow equivalent to the operation of the diode in a resonant circuit with appropriate elements.[86] Under such conditions, the dissipated DC power, P_{DC}, and the time-average AC power, P_{AC}, are evaluated and the conversion efficiency is calculated as $\eta = -P_{AC}/P_{DC}$. Therefore, negative values of η indicate a resistive behavior of the diode, while positive values mean AC generation from DC.

We want to remark that the values of the current I reported in this work have been usually normalized in such a way that its absolute value in A in a given device can be obtained just multiplying, in the case of the n^+nn^+ diodes, by the non-simulated dimension (in units of m), and, in the case of SSDs, by the experimental sheet electron density in the channel n_s (in units of m^{-2}).

II. CURRENT OSCILLATIONS ASSISTED BY OPTICAL PHONON EMISSION IN GaN n^+nn^+ DIODES

Under certain conditions, plasma instabilities associated with streaming motion of carriers taking place in n^+nn^+ diodes can lead to current oscillations.[21,22] The origin of the phenomenon, known as Optical Phonon Transit Time Resonance (OPTTR), is characterized by a frequency related to the transit time between consecutive optical phonon emissions (OPEs) by electrons along the active region of the diode. While the phenomenon has been previously studied essentially in InN, InP and GaAs n^+nn^+,[23,29,89-96] in this chapter we will deal, by means of Monte Carlo (MC) simulations, with the case of gallium nitride (GaN) diodes.

Experimental evidences of this phenomenon are humps observed in the *I*-*V* curves of diodes based on InSb,[97] GaAs,[98] InGaAs[99] e InP[100] at cryogenic temperatures when the applied voltage reaches the threshold for one, two and three optical phonon emissions. As ultimate confirmation of the OPTTR, the generation of millimeter-wave radiation in InP with a frequency following the characteristic bias dependence of the process has been detected.[101] To date just some singular points in the derivative of the *I*-*V* curve of a GaN TLM at 7 K have been observed.[15]

The aim of this chapter is to study the optimum conditions for the onset of OPTTR induced current oscillations in GaN n^+nn^+ structures by modifying parameters like the temperature, applied voltage, and doping and length of the *n* region. Simulations show that current oscillations at frequencies in the terahertz range can be obtained at very low temperatures. Moreover, by choosing the appropriate applied voltage and length of the *n* region, some degree of tunability can

be achieved for frequencies close to the plasma frequency of the *n* region of the n^+nn^+ diode.

The content of the chapter is structured as follows. In section II.1 the OPTTR phenomenon and the conditions for obtaining oscillations are explained, and in section II.2 the main results obtained in bulk GaN and n^+nn^+ diodes, already published in Ref. 102, are shown and discussed.

II.1. OPTTR: concept and conditions

II.1.a. Single particle

In a III-V semiconductor material at very low temperature the absorption of optical phonons is basically absent, while OPE is the dominant scattering mechanism electrons suffer. In these conditions, the dynamics of an electron subjected to a constant electric field E is very simple. The carrier is ballistically accelerated by the field until reaching the energy necessary for emitting an optical phonon ($\hbar\omega_0$). Then, the OPE takes place, so that the electron loses practically all its energy and stops. Next, there will be another acceleration and the consequent stop when emitting the following optical phonon. Obviously, this dynamics is repeated throughout the whole material, as seen in Figure 9, and gives rise to a clear modulation in the value of the velocity of every single electron. This process is spatially periodic with a characteristic length given by

$$l_0 = \frac{\hbar\omega_0}{eE}, \tag{1}$$

where e is the electron charge; and it is also periodic in time with a period, called transit time, which can be written as

$$\tau_E = \sqrt{2m_0 m^* \hbar\omega_0} \Big/ eE, \tag{2}$$

where m^* and m_0 are the effective and free electron masses, respectively.

In fact, the main interest of this phenomenon is that its characteristic frequency,

$$f_E = 1/\tau_E, \tag{3}$$

lies within the terahertz range. For this reason, the exploitation of OPTTR to obtain current oscillations of such high frequency is of great interest and deserves further

investigation. Moreover, if the optical phonon energy of the material is high, the phenomenon occurs more significantly because of the stronger modulation of velocity. This is the case of GaN, for which $\hbar\omega_0$=0.091 eV.[103]

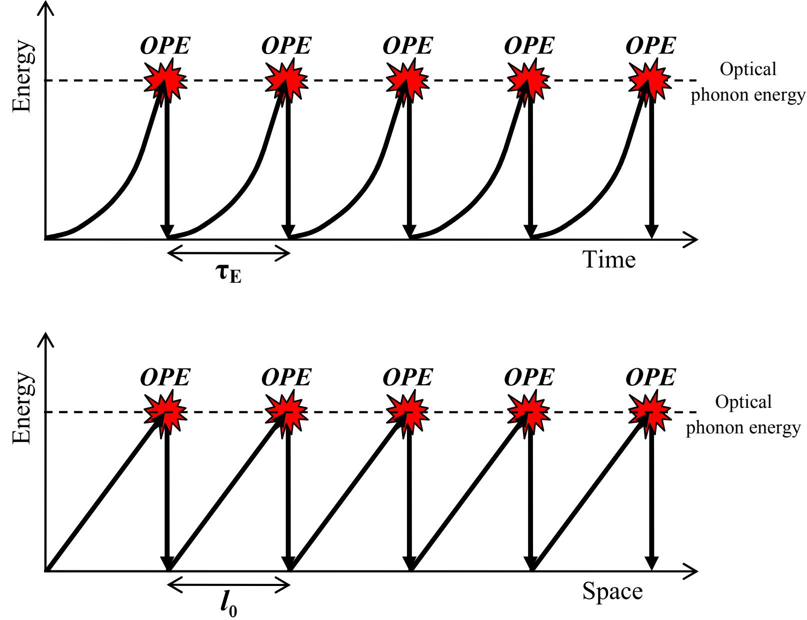

Figure 9. Scheme of the optical phonon emission (OPE) for an electron in the (a) time and (b) space domains.

II.1.b. Collective phenomenon

If we now consider a real device with a large amount of electrons, the stopping processes will lead to carrier accumulations, thus giving rise to a non-uniform electric field.

Achieving oscillations in the current within a device requires that the OPTTR process takes place in a coherent (and therefore collective) way, i.e., the phonon emissions must be synchronized by means of the self-consistent electric field. This phenomenon will inevitably be influenced by the parameters characterizing the electronic plasma, which will establish some conditions for the oscillations to appear.

Firstly, carrier accumulations can reinforce the spontaneous charge oscillations taking place in the semiconductor at the plasma frequency,

$$f_p = \frac{e}{2\pi}\sqrt{\frac{N}{m^* m_0 \varepsilon_0 \varepsilon_r}}, \tag{4}$$

where N is the impurity concentration and ε_0 and ε_r are the vacuum and relative permittivity, respectively.[104] When $f_E \approx f_p$, a feedback process of the OPPTR phenomenon takes place by means of the electric field fluctuations, so that relevant current oscillations of frequency f_E are possible.

Additionally, for the feedback action of the electric field to be effective, a minimum distance between electron accumulations $l_{0_{min}}$ must exist, in such a manner that long-range Coulomb interaction between adjacent carrier accumulations can be strong enough. The value of $l_{0_{min}}$ should be related to the Debye length[105] of the material

$$\lambda_D = \sqrt{\frac{k_B T \varepsilon_0 \varepsilon_r}{Ne^2}}, \qquad (5)$$

k_B being the Boltzmann constant. As will be observed in the results of the simulations, $l_{0_{min}}$ must be several times longer than λ_D for the oscillations to appear.

Finally, it is also necessary that electrons start the process with a very low velocity dispersion, condition that can be achieved in n^+nn^+ diodes where the doping of the n^+ and n region are sufficiently different, because of the high potential barrier that electrons find when they are injected into the n region.

II.2. Monte Carlo simulations and results

We have analyzed the OPTTR in GaN n^+nn^+ diodes by means of the tool described in the previous chapter. It is important to underline that since these diodes are vertical structures, dislocations are essentially parallel to electron transport and therefore this scattering mechanism has a negligible influence on the results.

II.2.a. OPTTR in bulk GaN

Using a single particle simulator, we have initially analyzed the conditions under which the electron dynamics is dominated by the OPPTR. To this end, velocity sequences of a single electron travelling in bulk GaN under the action of a constant electric field have been calculated at different temperatures, as shown in Figure 10 for an electric field of 2 kV/cm.

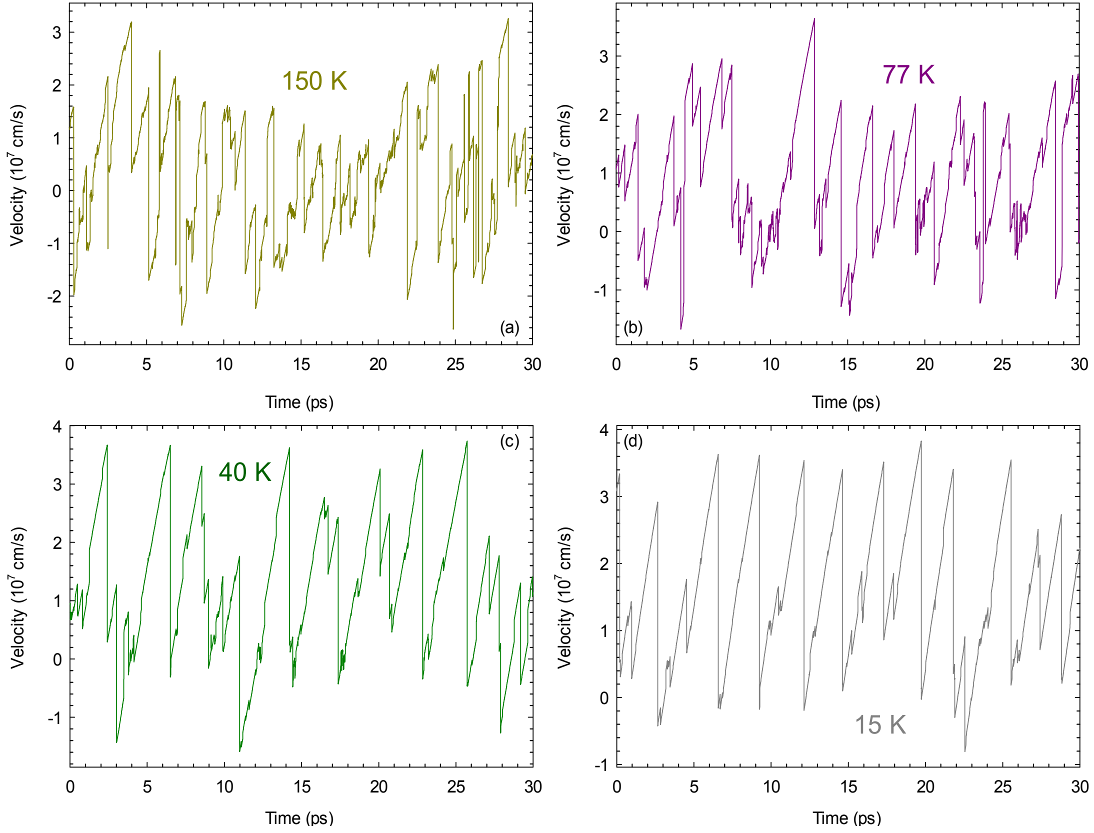

Figure 10. Sequences of instantaneous velocity of a single electron under the action of an electric field of 2 kV/cm at different temperatures (a) 150 K, (b) 77 K, (c) 40 K y (d) 15 K in GaN (doped 10^{15} cm^{-3}).

At very low temperature, 15 K [Figure 10(a)], the velocity sequence exhibits a periodic behavior quite similar to what explained before for the OPPTR dynamics: accelerations and subsequent stops when emitting the optical phonons. The period of the velocity oscillations observed in the sequence is slightly longer than the theoretical one, given by equation (2). This is due to the influence of other scattering mechanisms also taking place at low temperature (acoustic phonons, ionized impurities and piezoelectric scattering), recognized in the plot as small instantaneous reductions of velocity. However, due to the essentially elastic and anisotropic (small velocity deviation) character of these collisions, their influence is practically negligible and it is OPE which dominates carrier dynamics. As temperature increases [Figure 10(b)-(d)], other scattering mechanisms compete more and more with OPE, especially the onset of optical phonon absorption, and thus the electron motion progressively loses its periodic behavior (practically undetectable beyond 40 K). The mechanism of absorption of optical phonons can be clearly identified by abrupt increases of velocity, already present at 77 K and quite frequent at 150 K.

II.2.b. n^+nn^+ diodes: reference structure

The simulated GaN n^+nn^+ diodes (see Figure 11) have a low doped n region of length L sandwiched between two 50 nm n^+ layers, with a doping two orders of magnitude higher than the n region. Ohmic contacts are considered in the n^+ regions at the boundaries of the diodes. L and n will be varied in the calculations to identify their influence on the results.

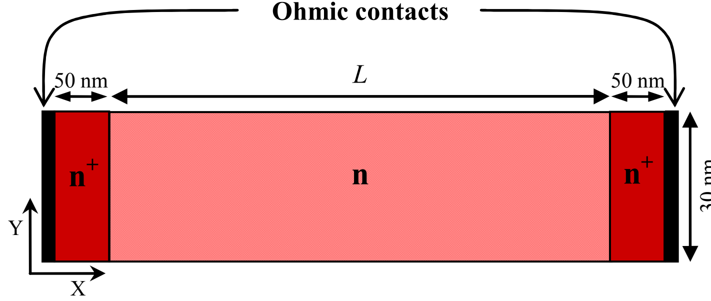

Figure 11. Scheme of the simulated GaN n^+nn^+ diodes.

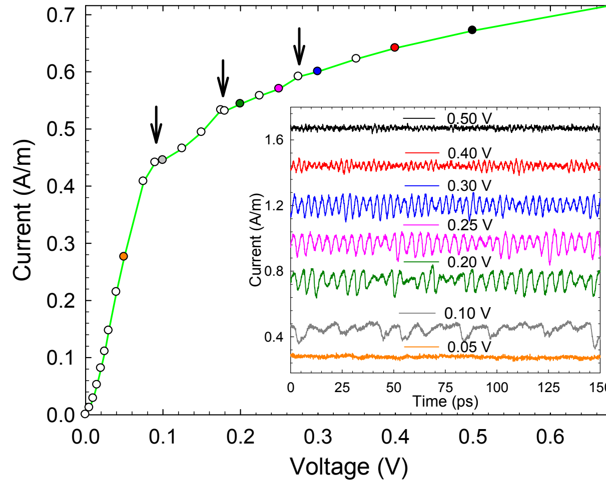

Figure 12. *I-V* curve, calculated at 15 K, of a GaN n^+nn^+ diode with a doping/length of the n^+ and n regions of 10^{17} cm^{-3}/50 nm and 10^{15} cm^{-3}/2 μm, respectively. The arrows indicate the bias points at which electrons reach the energy to undergo one, two and three OPEs while crossing the n region. The inset shows the time evolution of the current for different voltages. In order to improve the readability, the curves are vertically shifted by 0.2 A/m each, starting from the one corresponding to V=0.2 V.

Figure 12 shows the *I-V* curve of a GaN n^+nn^+ diode with an n region of length L=2 μm and doping 10^{15} cm^3 calculated at 15 K, which is the structure of reference to be compared with diodes where some of these parameters will be modified. When the applied voltage reaches the threshold for one OPE, which is $\hbar\omega_0/e$=0.091 V, and also at twice and three times such a value, the curve shows unusual humps, as found

experimentally in diodes made of other materials. Moreover, as observed in the current sequences of the inset, the current exhibits an oscillatory behavior in the bias range from 0.1 to 0.5 V approximately.

To understand the phenomenon, profiles of OPE rate and electric field along the diode for different applied voltages are shown in Figure 13. As observed, due to the localized injection of low-energy carriers in the n region at the source n^+n interface, the emissions take place also at localized, spatially-periodic regions [Figure 13(a)], where carriers stop. The associated electron accumulations at these stopping regions give rise to the so-called spatial free carrier grating, with the consequent inhomogeneity of the electric field profile [Figure 13(b)]. An increasing number of (closer) emission zones are observed as the applied voltage increases, the distance l_0 between them correctly following equation (1).

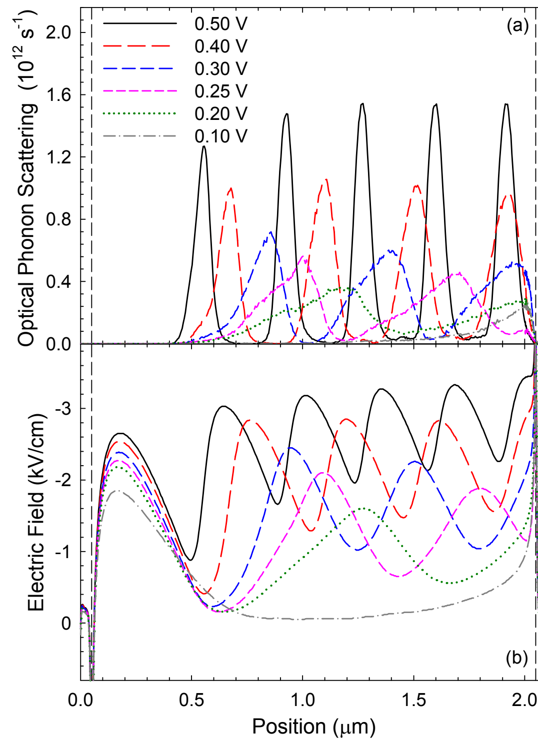

Figure 13. Profiles of (a) OPE rate and (b) electric field along the diode of Figure 12 at 15 K for different voltages.

At first sight it may seem that there are no significant qualitative differences between the curves of Figure 13(a): all of them show the expected spatially periodic behavior, the number of stop zones being equal to the integer part of the ratio $eV/\hbar\omega_0$. But, actually, there is a very significant difference: while for low voltages the emission regions are more spread out, as the voltage increases, the profiles show

a more defined shape, with a clear localization of the emission regions. This feature is key for determining the presence or absence of current oscillations.

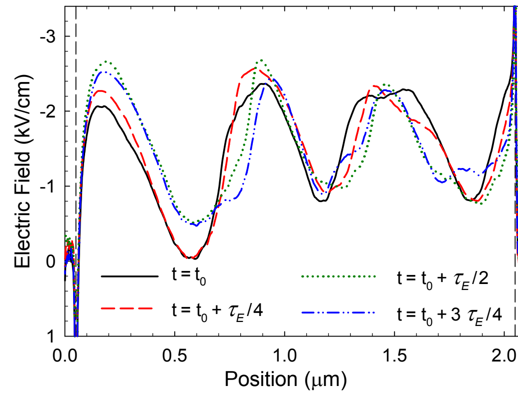

Figure 14. Profile of electric field for several equidistant times within one period of oscillation for an applied voltage V=0.3 V in the diode of Figure 12. The temperature is 15 K.

As explained in the previous section, to have current oscillations in the diode it is necessary to synchronize in time the OPEs taking place at different positions in the active region, what is only possible through the feedback provided by the self-consistent electric field. Figure 14 shows the electric field profile at several equidistant times within one period of oscillation for the case of V=0.3 V. When an OPE occurs at a given position, a local increase of electron concentration takes place, which couples to the electric field, leading further OPEs to be delayed in time and shifted in space, thus originating the observed current oscillations. To provide this synchronizing feedback, the profile of the electric field evolves in time during the period of the oscillation as observed in Figure 14, thus originating the spread out shape of the time-average profiles of Figure 13(a) in the case of applied voltages for which clear oscillations are observed in the current. As the applied voltage increases, the separation between accumulation regions l_0 decreases, becoming shorter than the minimum distance $l_{0_{min}}$ necessary to have a feedback of the electric field strong enough to synchronize the OPEs taking place at different positions. For instance, in the case shown in Figure 13, when l_0 becomes shorter than about 20 times the Debye length corresponding to the doping of the n region, the current oscillations practically disappear (that happens for V>0.4 V, see Figure 12). In such cases, there is no time evolution of the electric field profile and clearly localized emission zones are observed in Figure 13.

The spectral analysis of the current sequences obtained from MC simulations evidences the presence of a clear peak in the spectral density of current fluctuations at the fundamental frequency of the oscillations, and also lower peaks at its first harmonics. The dependence of the fundamental frequency on the applied bias, shown in Figure 15, follows closely the theoretical estimation provided by equation (3), with $E=V/L$. Regarding the amplitude of the oscillations, its maximum value is achieved around the plasma frequency of the n region, 0.2 THz in this case, which confirms the important role played by plasma oscillations in the feedback process by the electric field.

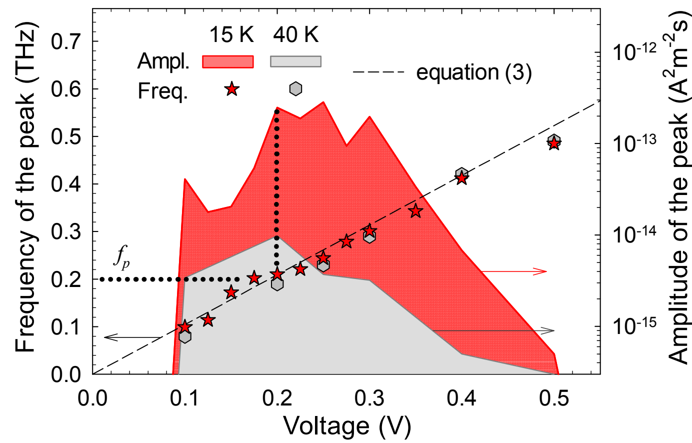

Figure 15. Frequency of the oscillations and amplitude of the corresponding peak in the spectral density (left and right axes, respectively) as a function of the applied voltage in the diode of Figure 12 at 15 K and 40 K. The theoretical oscillation frequency given by equation (3) is also plotted.

II.2.c. n^+nn^+ diodes: temperature influence

When the temperature is increased to 40 K, current oscillations are much weaker than for 15 K and the bias range with significant current oscillations extends only up to 0.3 V (Figure 15). This is due to two reasons. On the one hand, by increasing temperature other scattering mechanisms become more probable and compete with OPE [see Figure 10(c)], the coherence of the phenomenon being degraded. And, on the other hand, the Debye length increases with temperature, so that the range of voltages for which l_0 is longer than $l_{0_{min}}$ (approximately twenty times the value of the Debye length) is shorter. The frequency of the oscillations f_E coincides with the case of lower temperature, following the theoretical value given by equation (3) independently of temperature. If the temperature is further increased

to 77 K, the OPTTR practically disappears and no current oscillation is observed, whereas the free carrier grating becomes fuzzier.

II.2.d. n^+nn^+ diodes: length influence

By varying the length of the n region L (keeping T=15 K), the results shown in Figure 16 and Figure 17 are obtained. When L is reduced to 1 µm (Figure 16), oscillations take place only up to around 0.225 V, which means a maximum of two OPEs along the n region [Figure 17(a)]. The amplitudes of the peaks in the spectral density are much smaller than for L=2 µm and the frequencies are somewhat below the theoretical prediction. If L is further reduced to 0.5 µm, current oscillations do not appear at all. For L=3 µm, current oscillations are present in a much wider bias range (0.1-0.6 V), giving place to more stop zones along the n region [Figure 17(b)]. Additionally, the frequency versus bias curve (Figure 16) shows a good agreement with the behavior predicted by equation (3) and the amplitude of the peaks is similar to the case of L=2 µm. Note that by increasing L the frequency of the oscillations taking place for a given applied voltage is lower, since it scales with the value of the electric field (inversely proportional to L). Again, for all the values of L the maximum amplitude of the oscillations corresponds to frequencies close to that of the plasma.

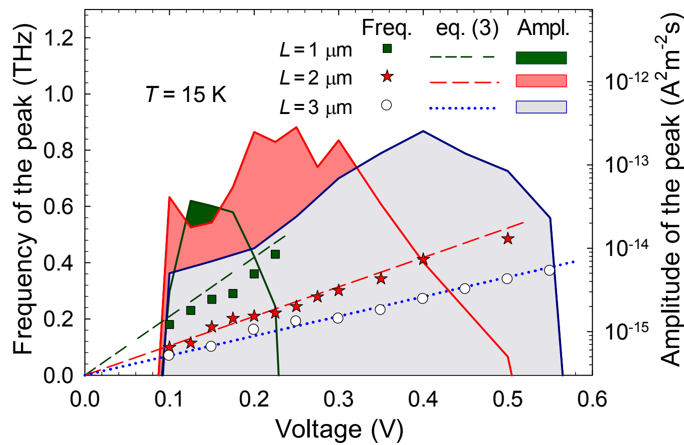

Figure 16. Frequency of the oscillations and amplitude of the corresponding peak in the spectral density as a function of the applied voltage for different lengths of the n region (doped 10^{15} cm^{-3}) at 15 K. The theoretical oscillation frequencies for each case are also plotted.

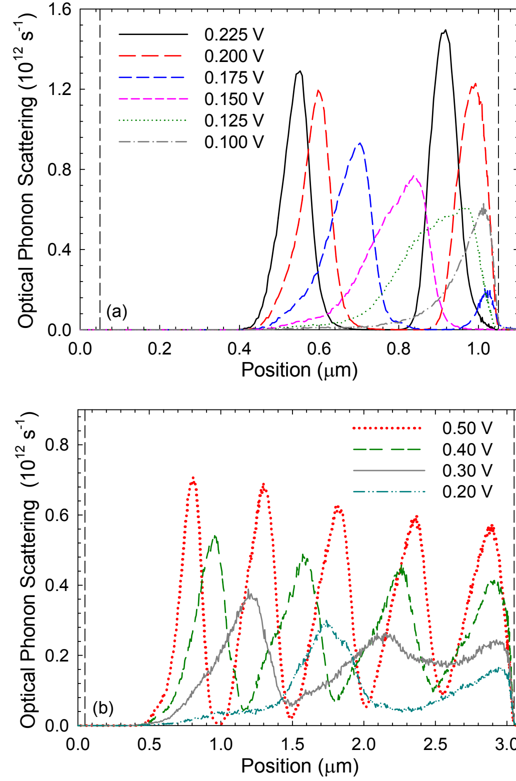

Figure 17. Profile of OPE rate at 15 K for different lengths of the *n* region (doped 10^{15} cm^{-3}) at 15 K: (a) L=1 μm and (b) L=3 μm.

From the last results it can be concluded that by varying the length of the *n* region the voltage range where current oscillations are present is modified, and also the amplitude of the peaks may change, but the maximum attained frequency is similar in all cases. To increase the frequency range of the oscillations induced by the OPTTR, the most straightforward possibility is to use n^+nn^+ structures with larger doping, where oscillations are expected to be sustained up to higher frequencies because of the increased plasma frequency.

II.2.e. n^+nn^+ diodes: doping influence

Figure 18(a) presents the results (at 15 K) for diodes with a doping one order of magnitude higher than in the previous structures both in the *n* and n^+ regions (10^{16} and 10^{18} cm^{-3}, respectively) and two different lengths (L=1 μm and L=2 μm). Space charge effects are obviously enhanced by the higher doping, thus providing oscillations with larger amplitude, especially in the shorter diode. Moreover these oscillations persist up to higher voltages as compared to the corresponding results with the same length and lower doping. This is due to the smaller value of the Debye length at increasing doping [equation (5)] and the shorter associated $l_{0_{min}}$. Now, the

plasma frequency of the n region is 0.64 THz and this allows obtaining significant current oscillations with frequencies above 1 THz, which constitutes the most remarkable result of this work.

Figure 18(b) shows the profile of OPE rate for V=0.9 V in the diode with L=2 μm. Nine stop zones are clearly visible. As observed, the amplitude of the modulation decays along the n region [also happening in Figure 17(b) for a high number of stop regions]. This is probably the reason why the amplitudes of the peaks for L=2 μm shown in Figure 18(a) are not as high as for L=1 μm. When L increases it is not possible to get a perfect synchronization of such a high number of OPEs along the n region, since the probability of having scattering mechanisms other than OPEs increases.

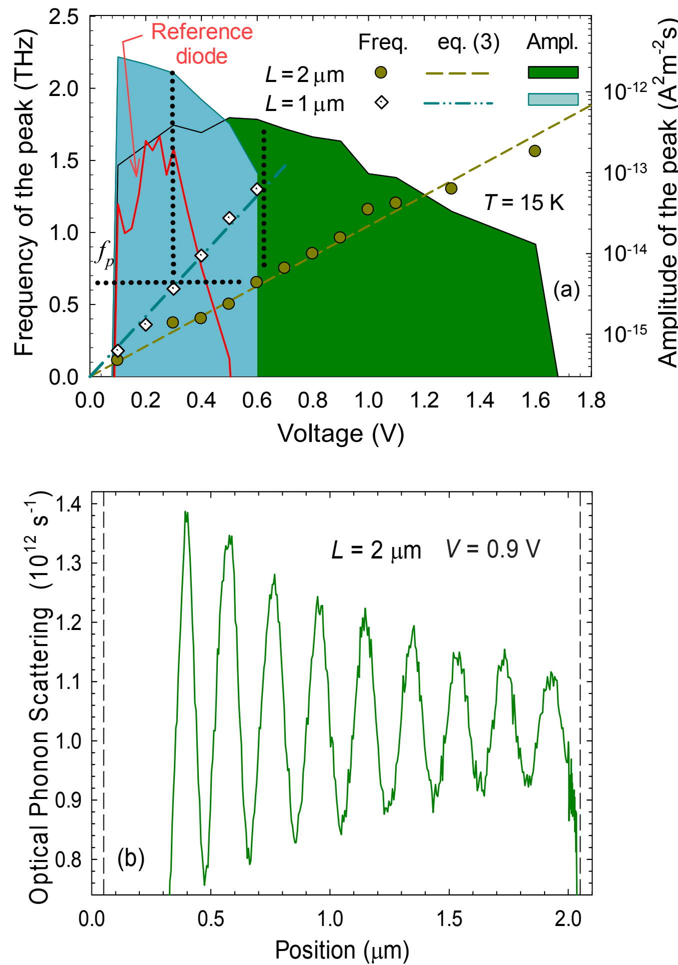

Figure 18. (a) Frequency of the oscillations and amplitude of the corresponding peak in the spectral density as a function of the applied voltage for two diodes with high doping (n^+=10^{18} cm^{-3} and n=10^{16} cm^{-3}) and different length (L=1 and 2 μm) at 15 K. In order to compare the results, the amplitude of the peak in the diode of Figure 12 (L=2 μm) is also plotted. (b) Profile of OPE rate in the diode with L=2 μm for V=0.9 V.

III. GUNN OSCILLATIONS IN GaN SSDs

This chapter constitutes the second main section of this dissertation and deals with the study of the capabilities of Self-Switching Diodes (SSDs) to operate as generators of THz signals. The SSD is a very simple two-terminal unipolar nanometric structure. It is realized by tailoring the boundary of a narrow semiconductor channel by means of two L-shaped trenches as shown in Figure 19. For the main objective here of conquering the THz gap we propose to exploit Gunn oscillations in SSDs. The planar topology, which improves heat dissipation and emission capability, and design flexibility of these diodes are important advantages with respect to standard (n^+nn^+) vertical structures. In addition, gallium nitride (GaN) is used to take advantage of its excellent properties for high-frequency and high-power applications, like its high values of threshold and breakdown electric fields, and saturation electron velocity.

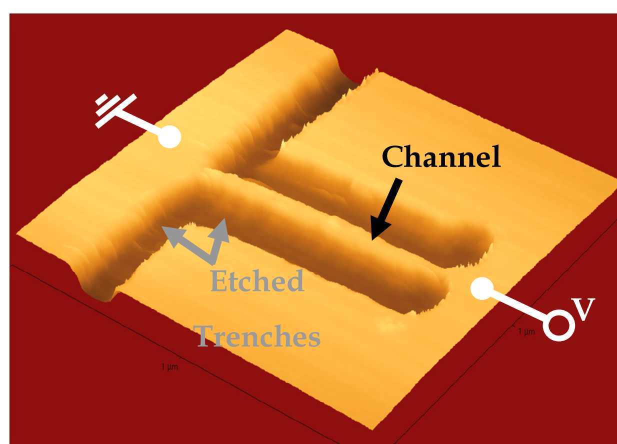

Figure 19. Atomic Force Micrograph (AFM) of a SSD.

The content of this chapter is structured as follows. First, in section III.1 a brief summary of the main milestones in the short history of the SSD and the Gunn effect

physics are provided. Then, the results are presented and discussed following the chronological order in which they were obtained, as summarized in Figure 20. Section III.2 presents initial Monte Carlo (MC) simulations, carried out with a constant surface charge model, where the influence of some characteristic parameters (both geometrical and of the model) are analyzed. In following sections we carry out a comparison of the simulations results with the experimental ones measured in devices from different fabrication runs: first batch in section III.3, second batch in section III.4 and third batch in section III.5. In this way we will illustrate the continuous interaction and feedback that has taken place in the time frame of this work between simulation and fabrication/characterization, this is, between our team and the colleagues in the IEMN (*Institut d'Electronique, de Microélectronique et de Nanotechnologie*) in Lille, where the GaN diodes are fabricated and characterized. After the first run we realized the need to implement in the simulator a more detailed model for the correct treatment of surface charge (the so called self-consistent surface charge model), an improved algorithm that has been of great help to design devices with the optimum geometry to experimentally attain THz generation.

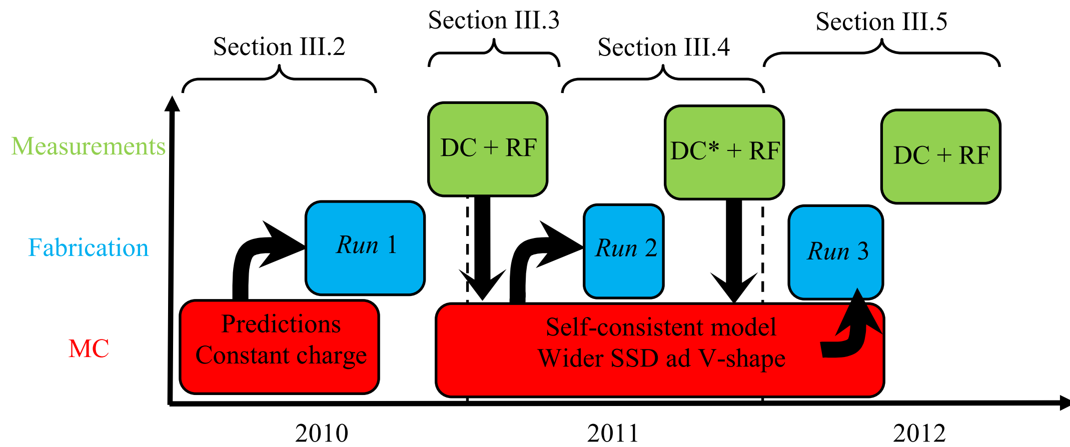

Figure 20. Work flow diagram. The asterisk means that the measurements were done by me during a research stay in Lille.

III.1. Literature review: SSDs and Gunn effect

III.1.a. Overview of the SSD

The device, invented in 2003 by A. M. Song,[27] was intended to perform logic operations. However, since then, this seemingly simple device has already demonstrated detection capability up to 110 GHz with a sensitivity of 75 mV/mW in

InGaAs,[106] up to 1.5 THz with a sensitivity of 300 mV/mW in GaAs,[107] both at room temperature, and even up to 2.5 THz at 150 K in InGaAs.[108] Also several groups, among them our research team, have studied the device based on InGaAs by means of MC simulations at different levels: static[75,109], dynamic[110,111] and noise[112,113] behavior, influence of temperature[114]; and also based on other materials like InAs or InSb.[115] In particular, related to the noise issue, a competitive value of the noise equivalent power of 62.5 pW/Hz$^{1/2}$ at 100 GHz[116] was achieved. Since the working principle is not based on ballistic transport, SSDs have also been fabricated in other materials like SOI,[117-119] thermoplastic polymers[120] or polycrystalline materials.[121] It is obvious that the emerging graphene will be the imminent next material for SSDs. In fact, several European groups are already working in applications for grants on this topic, where our team hopes to collaborate in the modeling packages.

In 2008 Xu K. Y. *et al.*[122] expanded the functionality of the SSD to a higher level. They predicted Gunn oscillations at 150 GHz for an SSD based on InGaAs. It is at this moment when our group started a research line on this topic and presented several contributions in international conferences.[123-125] In particular, by means of MC simulations, numerical estimations predicted high frequency oscillations up to 100 GHz for a 1.5 μm long SSD based InGaAs with a threshold of 2.5 V, and, for the first time in GaN, oscillations up to 400 GHz for a 1 μm long SSD with a threshold of 30 V were reported. Nowadays, the group (and me too since about the middle of the year 2010), motivated by the participation (as coordinator) in the *ROOTHz* project (*Semiconductor Nanodevices for Room Temperature THz Emission and Detection*), continue working on this research line. The final challenge is to design and fabricate a compact, cheap, room-temperature emitter/detector system approaching the THz range using GaN-based SSDs. Even if detection results are satisfactory, no experimental evidence of emission has been achieved yet, and more work is needed. In this context, the aim of this work has been to improve the MC modeling and study in detail the possibility of achieving THz oscillations by means of Gunn effect in GaN SSDs. Some of the obtained results have been published in Ref. 126.

Concerning the working principle of SSDs, the key point in the device is the etching of the insulating grooves providing an asymmetric shape in the two-terminal diode. In such a geometry an applied voltage V not only changes the potential profile along the channel direction, but also either widens or narrows the effective channel

W_{eff} depending on the sign of V. This results in a diode-like characteristic, but without the use of any doping junction or barrier structure, as can be inferred from Figure 21(a)-(c).[27,75]

The fabricated GaN-based SSDs do not show a clearly rectifying capability, which would be especially useful for detection purposes. The absence of clear rectification is not an obstacle, since the physical principle of Gunn oscillations is not based at all on the asymmetry of the I-V curve. In fact, the design rules are mainly directed to emission purposes, without paying too much attention to detection, already achieved in some specific geometries.

We can establish a similarity between this innovative planar diode and the standard vertical $n^+n^-nn^+$ structures[127] as shown in Figure 21(d)-(e). Here it becomes clear that Gunn oscillations are promoted by the particular shape of the SSD. The rupture in the symmetry originated by the vertical trenches creates a high field region at the beginning of the channel like that originated by the notch region (n^-) in the vertical diodes.

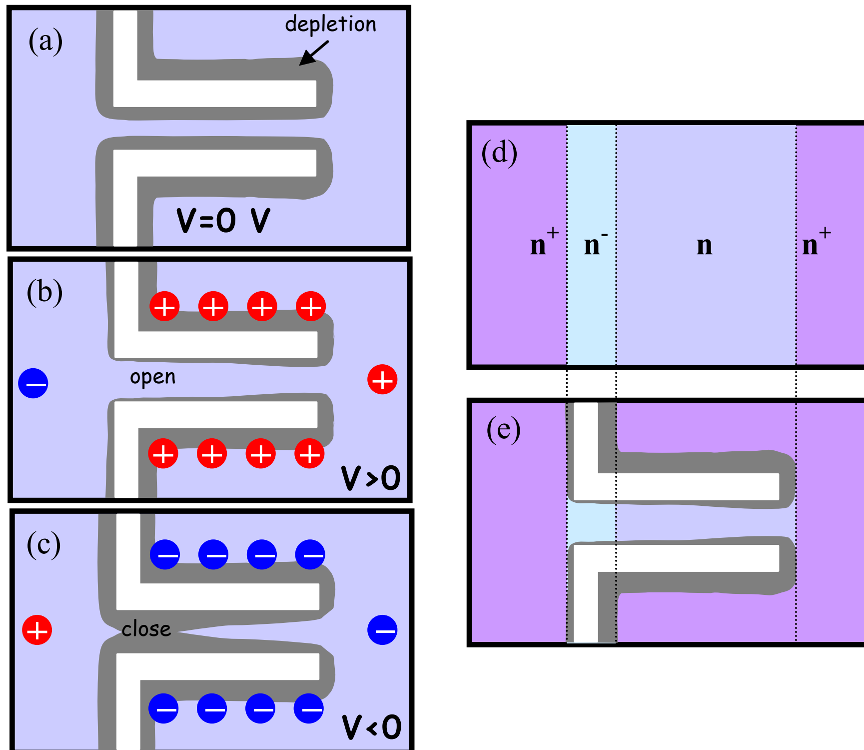

Figure 21. (a) Depletion region formed close to the etched boundaries in equilibrium. Depending on the sign of the applied voltage the effective channel width will be (b) increased or (c) reduced. Figures (d) and (e) illustrate the similarities between an $n^+n^-nn^+$ diode and the SSD geometry.

III.1.b. The Gunn effect

Since 1950 several researchers began to look for the presence of Negative Differential Resistance (NDR) in semiconductor devices with the aim of achieving oscillators and solid state amplifiers.[128-130] It was in 1963 when J. B. Gunn observed for the first time microwave current oscillations in homogeneous samples on n-type gallium arsenide (GaAs) and indium phosphide (InP) subjected to high electric fields.[24] After this experimental evidence and up today a lot of related work can be found in the literature, calling this mechanism Gunn effect.[131-139]

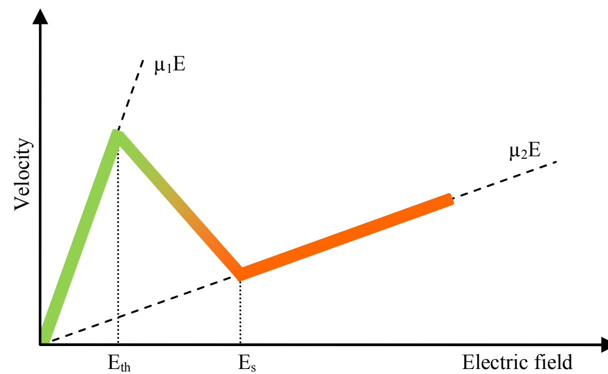

Figure 22. Scheme of the velocity-field curve with a negative slope region, NDR, for fields between E_{th} y E_s.

In some III-V compounds, for an electric field above a threshold level, the mobility of electrons decreases as the electric field is increased, thereby producing negative resistance (see Figure 22). Below the threshold field, E_{th}, the material acts as a passive resistance. However, above E_{th} the electron velocity decreases as the field increases, producing a region of NDR. This is the essential feature that leads to current instabilities and Gunn oscillations in an active device, and it is due to the special conduction band structure of some direct band gap semiconductors, as GaN.

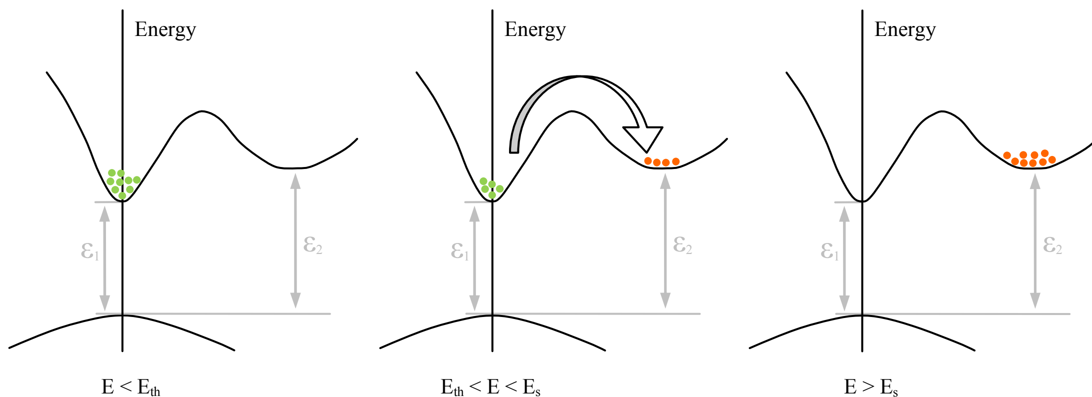

Figure 23. Electron transfer mechanism to higher valleys of lower mobility when increasing the electric field.

The basic physical mechanism responsible for the effect is the progressive transfer of hot electrons from high mobility valleys to low mobility valleys in the conduction band as the field increases, as shown in Figure 23. The resulting negative differential mobility makes the homogeneous electron distribution unstable. Narrow domains of extremely high field build up and propagate through the diodes.

A two-terminal device made from such a material can produce microwave oscillations, the frequency of which is primarily determined by the electron saturation velocity in the material and the length of the active region of the diode, and not by any external circuit. Figure 24 shows the advantages of using GaN as compared to GaAs and InP: higher breakdown and saturation fields, and higher saturation velocity. These features make GaN appropriate to generate oscillations of higher frequency and power than the other semiconductors.

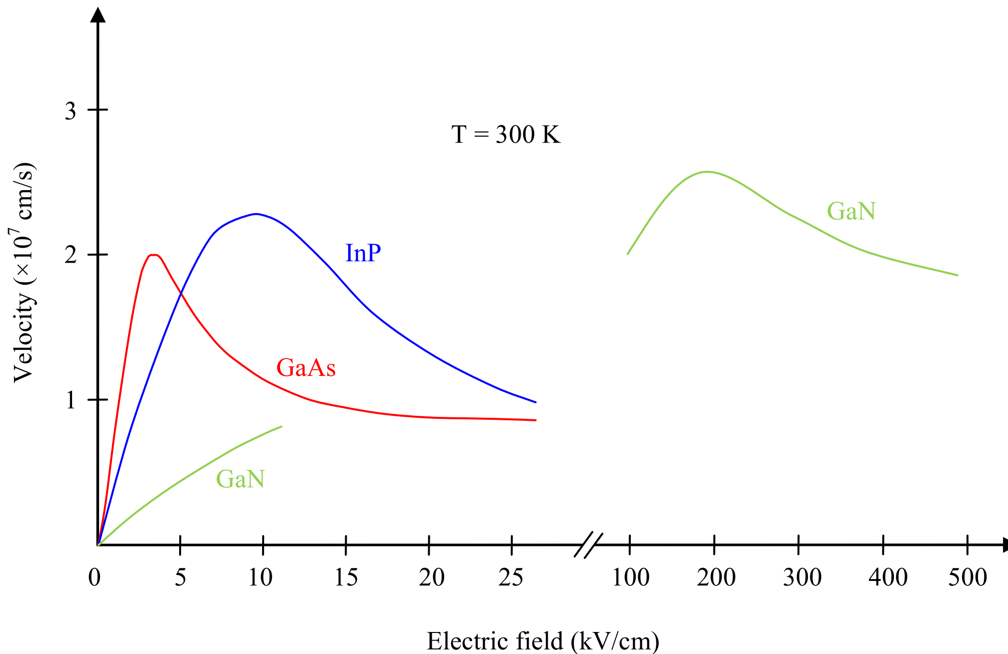

Figure 24. Velocity-field curves for InP, GaAs and GaN at room temperature.

III.2. Preliminary simulations with the constant surface charge model

Previously to the fabrication of the GaN SSDs we have performed simulations of different devices using the simple (and fast) constant surface charge model in order to study the ability of these nanodevices to generate Gunn oscillations at room temperature. We have used this simple model to analyze the influence of some characteristic parameters (both geometrical and of the MC model), in order to

identify the individual influence of each of them avoiding the complex effects arising when the surface charges are not constant. We will consider as reference structure a SSD with L=1 μm, W=150 nm, W_V=200 nm, W_H=100 nm, C=600 nm, a background doping N_{Db}=2×10^{17} cm^{-3} and a surface charge density σ = -0.75×10^{12} cm^{-2} [see Figure 7(b)]. As a general feature, this structure shows oscillations in the current when the applied voltage exceeds 50 V, originated by the classical Gunn effect, but no evidence of the onset of the oscillations is observed in the *I-V* curves as shown in Figure 25. The values of the current in these curves are obtained as the time average over long simulations, including a large number of periods when oscillations are present.

III.2.a. Influence of the model parameters (*σ* and N_{Db})

As the two critical parameters in our model are σ and N_{Db} (whose values are unknown and should be determined by comparison of simulated results with measurements), the first set of simulations analyzes the influence of these parameters. The *I-V* curves of the reference structure and time sequences of the current for an applied voltage of 50 V, for which this diode exhibits small-amplitude Gunn oscillations (around 300 GHz), are shown in the figure for several values of σ and N_{Db}. We recall that the current is normalized in such a way that its absolute value in A in a given device is obtained just multiplying the reported values by the experimental sheet electron density in the channel n_s (in units of m^{-2}). As expected, the higher the value of σ, the higher the induced channel depletion and the lower the current level, Figure 25(a). The frequency and amplitude of the oscillations also decrease, and even disappear for the highest σ due to the excessive channel depletion.

Concerning the influence of N_{Db} when σ is kept constant, the current is higher as N_{Db} increases because of the higher electron concentration, Figure 25(b). Additionally, the inset shows that the Gunn oscillations are reinforced by a higher N_{Db} due to a stronger feedback provided by the electric field, allowing the onset and development of such current oscillations. It is interesting to note that this also makes the oscillation frequency increase.

III.2.b. Influence of the temperature and geometric parameters

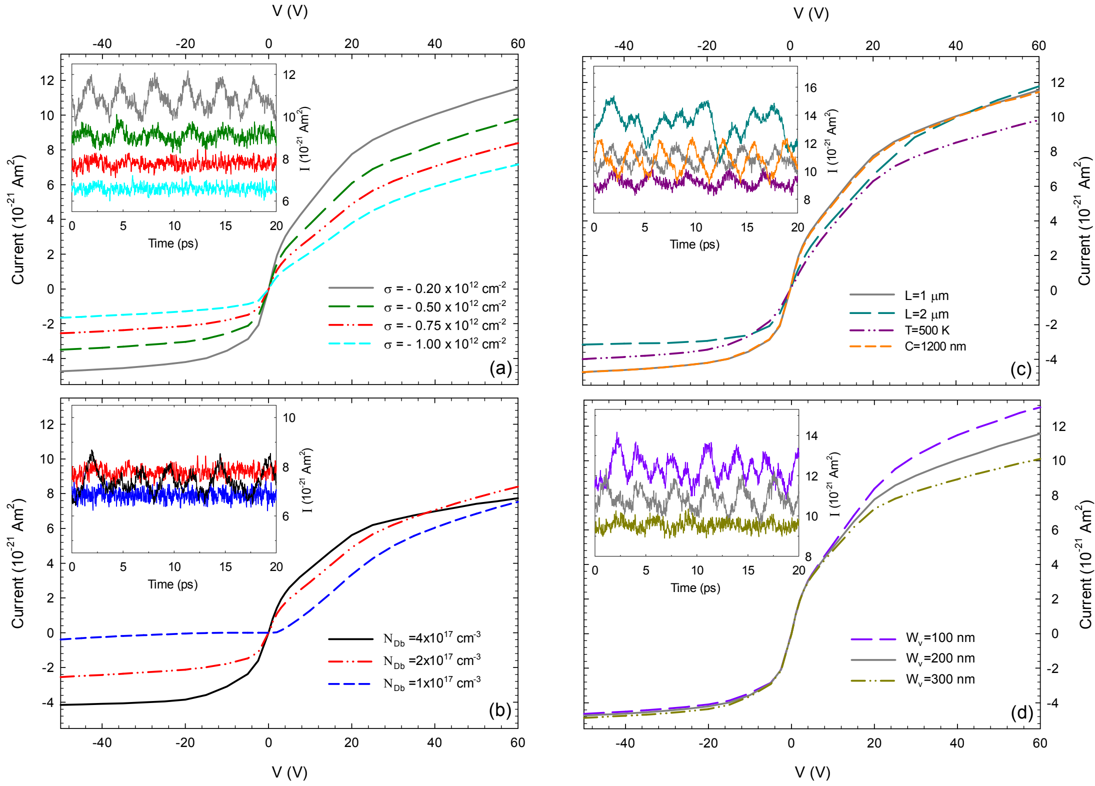

Figure 25. *I*-*V* curves of GaN SSDs (L=1 μm, W=150 nm, W_V=200 nm, W_H=100 nm and C=600 nm) when varying: (a) the surface charge density σ (for N_{Db}=2×10^{17} cm^{-3}) and (b) the background doping N_{Db} (for σ = -0.75×10^{12} cm^{-2}). More *I*-*V* curves of GaN SSDs (σ = -0.2×10^{12} cm^{-2}, N_{Db}=2×10^{17} cm^{-3}, W=150 nm, W_H=100 nm and C=600 nm) when varying (c) the channel length L (with W_V=200 nm) and (d) the width of the vertical trenches W_V (with L=1 μm). The cases T=500 K (with L=1 μm and W_V=200 nm), and C=1200 nm (with L=1 μm and W_V=200 nm) also plotted in (c). The plotted value of the current is obtained as the time average for long simulations, including a large enough number of periods when oscillations are present. The insets show current sequences calculated for an applied voltage of 50 V (100 V for L=2 μm).

The influence of the channel length, anode access region and operating temperature is presented in Figure 25(c). As observed, the oscillation frequency essentially scales with the channel length L (150 GHz for 2 μm), while the *I*-*V* curve is less affected. Just a change in the slope for low voltages is observed, while the same saturation current is reached for high forward voltages. The length of the anode access region C hardly influences neither the *I*-*V* curve nor the oscillations, since it is essentially an ohmic region of much lower resistance than the channel. We can confirm that, remarkably, Gunn oscillations still remain even with a strong heating of the diodes (uniform temperature of 500 K considered in the simulations), conditions expected to occur in these small devices in normal operation (under very high

voltages and large dissipated power). At 500 K only a drop of the electron velocity takes place, so that the current level lowers and the oscillation frequency decreases (from 300 to 260 GHz).

Finally, by increasing the width of the vertical trenches W_V [Figure 25(d)], oscillations with lower amplitude and frequency are found, as well as a lower saturation current. This is due to the fact that by enlarging W_V a shorter portion of the channel is controlled by the anode voltage (which contributes to the appearance of the oscillations by means of the increase of carrier concentration in the channel).

III.2.c. Study of the efficiency

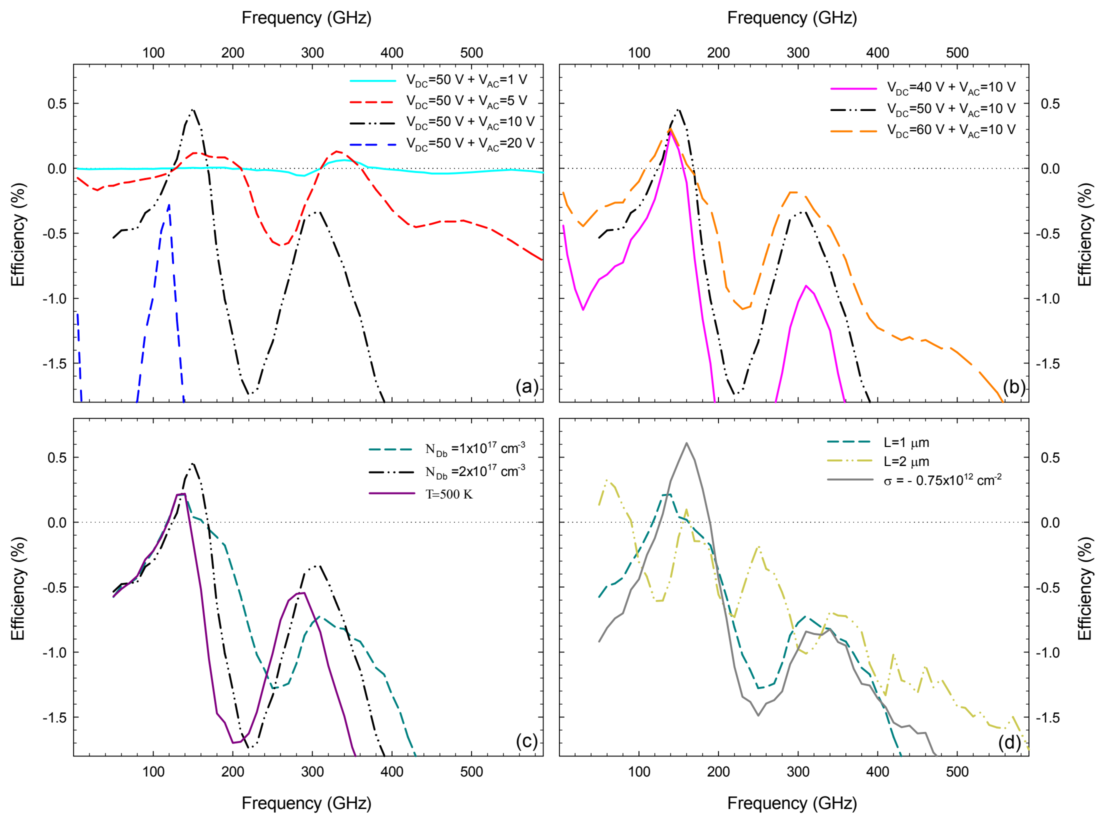

Figure 26. DC to AC conversion efficiency η as a function of the frequency of the AC excitation when varying: (a) the AC bias conditions (V_{DC}=50 V), (b) the DC bias conditions (V_{AC}=10 V), (c) background doping N_{Db} and temperature T and (d) channel length L and surface charge σ (N_{Db}=1×10^{17} cm^{-3}). Unless otherwise indicated, L=1 μm, W=150 nm, W_V=200 nm, W_H=100 nm, C=600 nm, σ = -0.2×10^{12} cm^{-2}, N_{Db}=2×1017 cm^{-3}, and T=300 K. In (c) and (d) V_{DC}=50 V and V_{AC}=10 V (except for the case L=2 μm, for which V_{DC}=100 V and V_{AC}=20 V).

In order to analyze the performance of SSDs operating as emitters, the DC to AC conversion efficiency, η , has been evaluated by means of the superposition of a single-tone sinusoidal potential of amplitude V_{AC} to a DC bias V_{DC}. The dependence

of η on the frequency of the AC excitation when varying several parameters is shown in Figure 26 and Figure 27. We have firstly considered four different values for V_{AC} (1, 5, 10 and 20 V) keeping constant $V_{DC} = 50$ V [Figure 26(a)], and then used a variable V_{DC} (40, 50 and 60 V) while V_{AC} is set at 10 V [Figure 26(b)]. Several bands of AC generation, with a usual maximum efficiency between 0.1 and 0.5 %, are observed at the fundamental frequency of the Gunn effect and also at around double frequency. Even if these values are not very high, as GaN diodes are able to support a large DC power, the AC power they can deliver could still be of practical use at such high frequencies.

As expected, the efficiency depends on the amplitude of both the DC and AC excitation. In particular, lower efficiency at generation bands of higher frequencies is observed for high amplitudes of AC excitation [see Figure 26(a)], while the opposite behavior is observed for the DC amplitude, i.e. higher efficiency is found for higher frequency bands as V_{DC} increases [see Figure 26(b)].

The influence of N_{Db}, L, T and σ on the efficiency is shown in Figure 26(c)-(d). Similarly to the previous results when just a DC excitation is applied, higher values of N_{Db} reinforce the oscillations, thus improving the efficiency. When increasing the temperature of operation a shift of the emission bands to lower frequencies takes place because of the smaller drift velocity of electrons at higher temperature, but the efficiency is not degraded. When comparing the efficiency for diodes with different channel lengths, wider emission bands are observed for shorter channels, with the frequency scaling as $1/L$. This result opens the possibility to increase the emission frequency of SSDs by reducing the channel length. Finally, a higher surface charge density σ, leading to a reduced W_{eff}, surprisingly provides higher efficiencies.

In all the cases, intriguingly, the frequency of the oscillations observed when the SSDs are biased with just a DC voltage (around 300 GHz for L=1 μm) lies within the second generation band and not the fundamental one (around 150 GHz) of the oscillations taking place in the presence of an additional AC bias.

III.2.d. Evolution of microscopic quantities

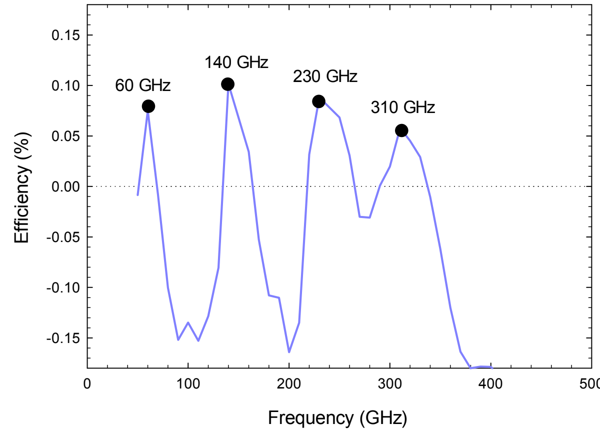

Figure 27. DC to AC conversion efficiency η as a function of the frequency of the AC excitation for a diode with L=2 μm, W=150 nm, W_V=300 nm, W_H=100 nm, C=600 nm, σ = -0.2×10^{12} cm^{-2}, N_{Db}=2×1017 cm^{-3}, and T=300 K. V_{DC}=100 V and V_{AC}=7 V.

In order to explain the previous results and to illustrate the microscopic processes leading to the presence of generation at different bands, we will study a diode where four emission bands are clearly identified, as shown in Figure 27. Figure 28 shows the profiles of carrier concentration and electric field along the center of the channel (i) at one given time for different frequencies of the AC excitation (at the center of each generation band), Figure 28(a)-(b), and (ii) at different equidistant time moments during one period of excitation with an AC signal of 310 GHz (central frequency of the fourth generation band), Figure 28(c)-(d). As observed, an increasing number (from 1 to 4) of charge domains (high field regions) drift along the channel for increasing frequencies of the AC excitation at the center of each generation band. These domains are originated by the transfer of electrons from the Γ_1 to U valleys (with higher effective mass) in the conduction band of GaN, as occurs in standard GaAs Gunn diodes. It is also noteworthy that the peak frequencies of the higher generation bands are not exactly integer multiples of the fundamental oscillation, because the formation of more than one accumulation domain increases the "dead space" (distance needed for the formation of the domain) at the entrance of the SSD.

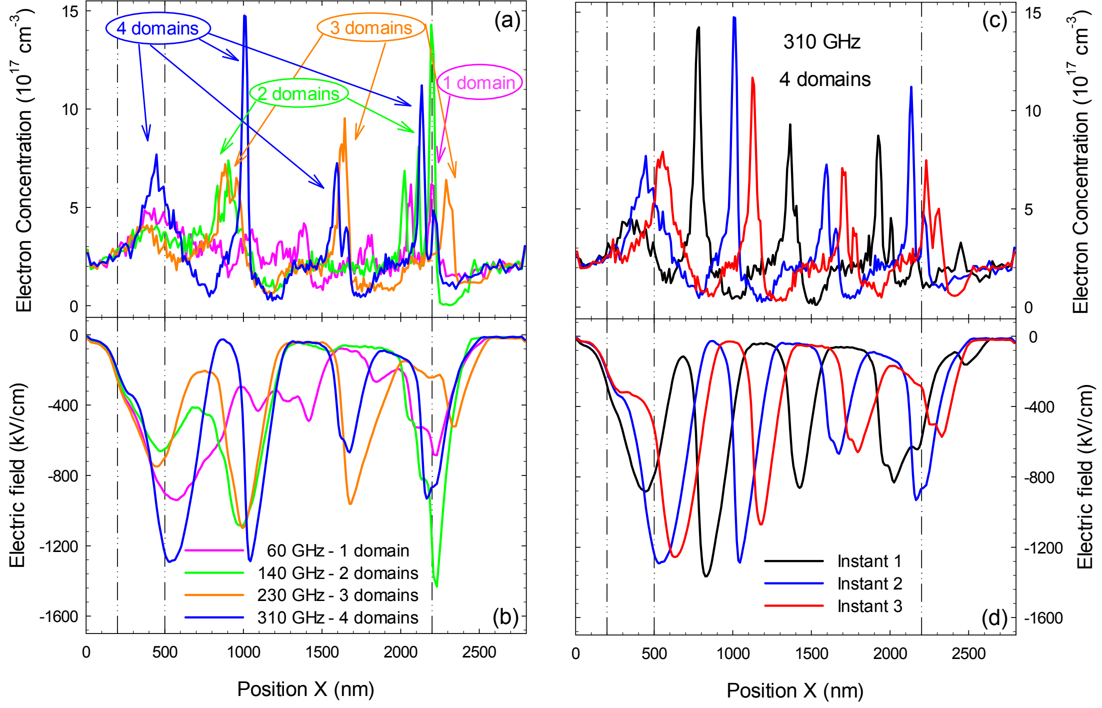

Figure 28. Profiles of (a) and (c) carrier concentration and (b) and (d) electric field along the center of the channel of an SSD at room temperature for V_{DC}=100 V and V_{AC}=7 V. Curves in (a) and (b) correspond to a given time within one period of the AC signal for frequencies at the center of the emission bands observed in Figure 27 (60, 140, 230 and 310 GHz). In (c) and (d) they correspond to equidistant time moments during one period of the AC excitation of frequency 310 GHz. The diode has L=2 µm, W=150 nm, W_V=300 nm, W_H=100 nm, C=600 nm, σ = -0.2×10^{12} cm^{-2} and N_{Db}=2×10^{17} cm^{-3}. Vertical lines indicate the position of the vertical trenches and the end of the channel.

The remarkably high values of the electric field observed in Figure 28 do not pose any problem for the correct simulation of the carrier dynamics even if the MC model does not include impact ionization processes, since the electron energy is not still high enough for generating a significant number of electron-hole pairs. Indeed, such electric fields are still well below the breakdown field of wurtzite GaN.

III.3. Comparison with experimental results of Run 1

III.3.a. First experimental measurements

In order to fix the value of the fitting parameters of the MC model, σ and N_{Db}, we have compared our simulations with experimental measurements obtained from the first run of GaN SSDs fabricated at the IEMN. The devices are made on an epitaxial layer consisting of 1.8 µm of undoped hexagonal GaN ([0001] orientation)

on a HR Si substrate, with a barrier of 23 nm of $Al_{0.3}Ga_{0.7}N$ and covered by 5 nm of SiN for passivation. We have decided to use GaN on Si because of its lower price, in spite of the poorer thermal conductivity since, as confirmed by the results shown in the previous section, heating should not be a critical issue for the onset of Gunn oscillations (even if the temperature increase has an important effect in the *I-V* curves). Measured values of sheet carrier density n_s in this epilayer are in the range 5-10x10^{12} cm^{-2}, with a mobility around 1200 cm^2/Vs. The fabrication process starts by depositing ohmic contacts (Ti/Al/Ni/Au, with a resistance of 0.3 Ω mm) and isolation by ionic implantation (He^+). Then, the etching of the trenches takes place (with a PMMA resist and ICP chlorine based technology), and finally the top metal layer (Ti/Pt/Au) is deposited for CPW line access. Several sizes and arrays of SSDs have been processed. A strong technological effort has been necessary in order to obtain a deep etch of 45 nm together with a small recess width (50 to 100 nm), as shown in Figure 29. Figure 29(a) is a SEM view of an array of 16 SSDs in parallel and Figure 29(b) a FIB cut view showing the shape of the trenches. We want to remark that this is a completely new technological process and these are the first ever SSDs fabricated on GaN.

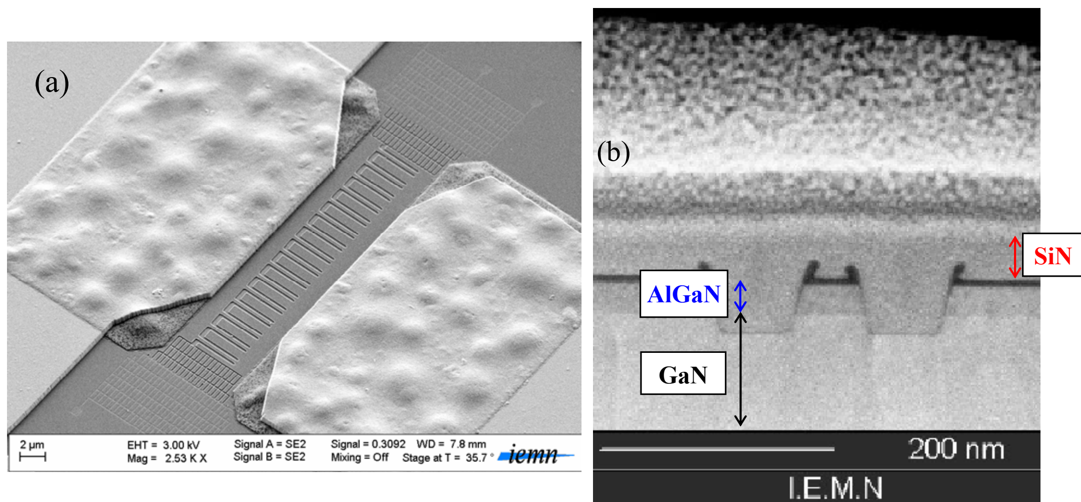

Figure 29. (a) SEM image of an array of 16 SSDs in parallel and (b) FIB cut view showing the shape of the recess.

The electrical characterization of several topologies (different number of channels in parallel: 1, 4, 16 and 32 SSDs) are shown in Figure 30. The correct linear law of the current versus the number of SSDs in parallel, inset of Figure 30(a), shows

that there is no apparent thermal limitation associated to the Si substrate. MC simulations also indicate that there is not a phase mismatch between the possible Gunn oscillations within the individual channels.[125] Moreover, the dependence of the *I*-*V* curves on the length and width of the channels, Figure 30(b), follows the trends observed in simulations, what validates the quality of the fabrication process. From these results we have estimated the width of the depletion region W_d, obtaining a value of 25±5 nm for both 1 μm and 2 μm channels.

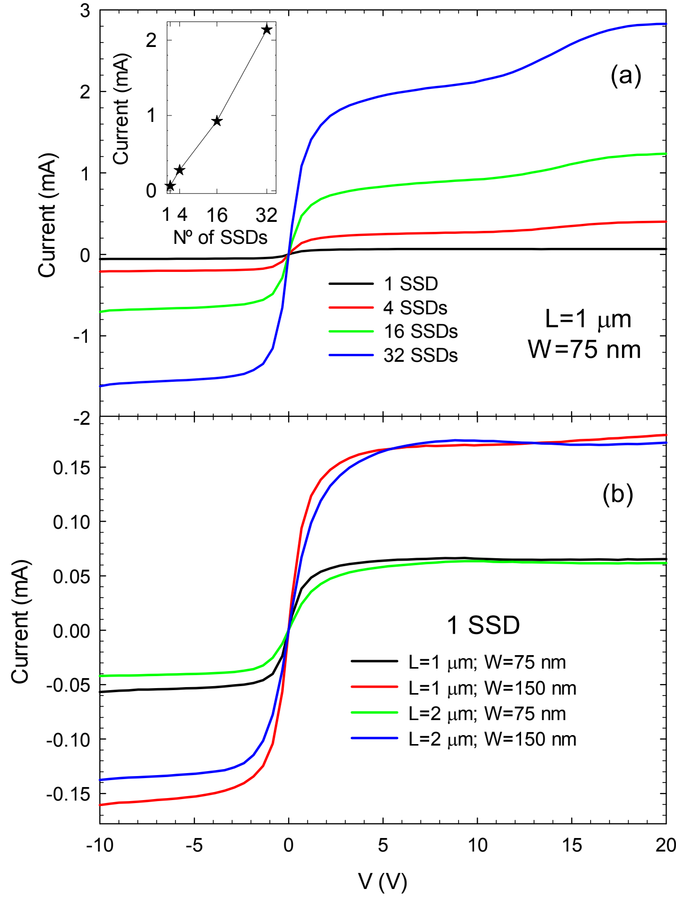

Figure 30. Experimental *I*-*V* characteristics of (a) arrays of SSDs with different number of diodes in parallel with L=1 μm, W=75 nm, and (b) a single SSD with different lengths and widths (all with W_V=100 nm, W_H=50 nm and C=400 nm). The inset in (a) shows the current for an applied bias of 10 V as a function of the number of SSDs in parallel.

III.3.b. Comparison with the constant surface charge model

Then, taking into account that $W_d = \sigma/N_{Db}$ within the constant surface charge model, we have performed simulations using several values of σ and N_{Db}, always providing a ratio of 25 nm. The obtained comparison with the experimental results is shown in Figure 31. As observed, for the lowest values of σ and N_{Db} it is possible to

fit the ohmic conductance (slope at low voltage), and for the highest values it is possible to obtain a similar saturation current (both for forward and reverse bias). However, there is no set of parameters able to correctly reproduce the whole *I-V* curve (even without keeping the ratio of 25 nm, results not shown here), thus indicating that the simple constant surface charge model used in these MC simulations is not adequate for the modeling of these devices.

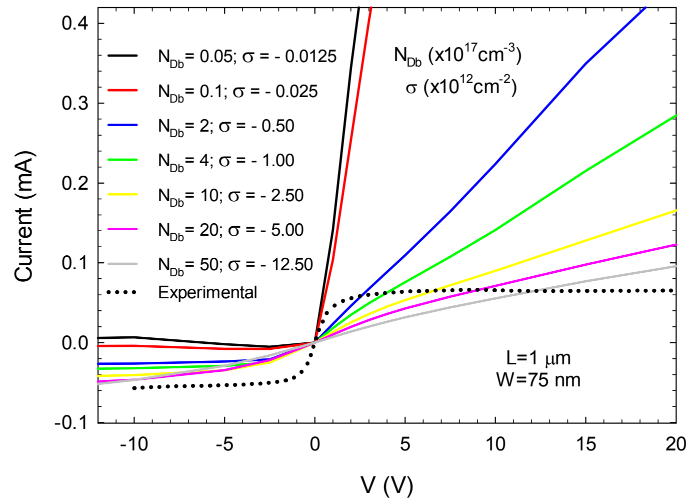

Figure 31. Comparison between measured and simulated *I-V* curves for a diode with L=1 μm and W=75 nm with different sets of values of N_{Db} and σ providing the same W_d=σ/N_{Db}=25 nm. A value of n_s=10×10^{12} cm^{-2} has been used.

III.3.c. Comparison with the self-consistent surface charge model

The fact that the constant surface charge model used so far in the simulations is unable to reproduce the experimental results indicates that the surface charge density along the boundary of the trenches is strongly non-homogeneous and voltage dependent, thus leading to the low saturation voltages and currents measured in the SSDs. Other possible reason for the discrepancies could be heating effects, not self-consistently considered in the MC simulations. As pointed out in section I.3, to account for the dependence of the surface charge on the position and applied voltage, the self-consistent model should be used. Figure 32 compares the MC results obtained for SSDs with L=1 and 2 μm and W=75 and 150 nm with the measured *I-V* curves in devices with the same geometry (N_{Db}=1×10^{17} cm^{-3} is considered). MC simulations are now able to satisfactorily reproduce the experimental behavior of the current, both for high-bias (saturation) and low-bias, and for SSDs with different values of channel length and width. Even if the low-voltage conductance and the

saturation current are not perfectly reproduced, the comparison is much more favorable than with the constant surface charge model. A more satisfactory fitting could be obtained considering the exact dimensions (an underetch of about 20 nm has been detected in the SEM images of the devices) instead of the nominal ones used in the CAD tool.

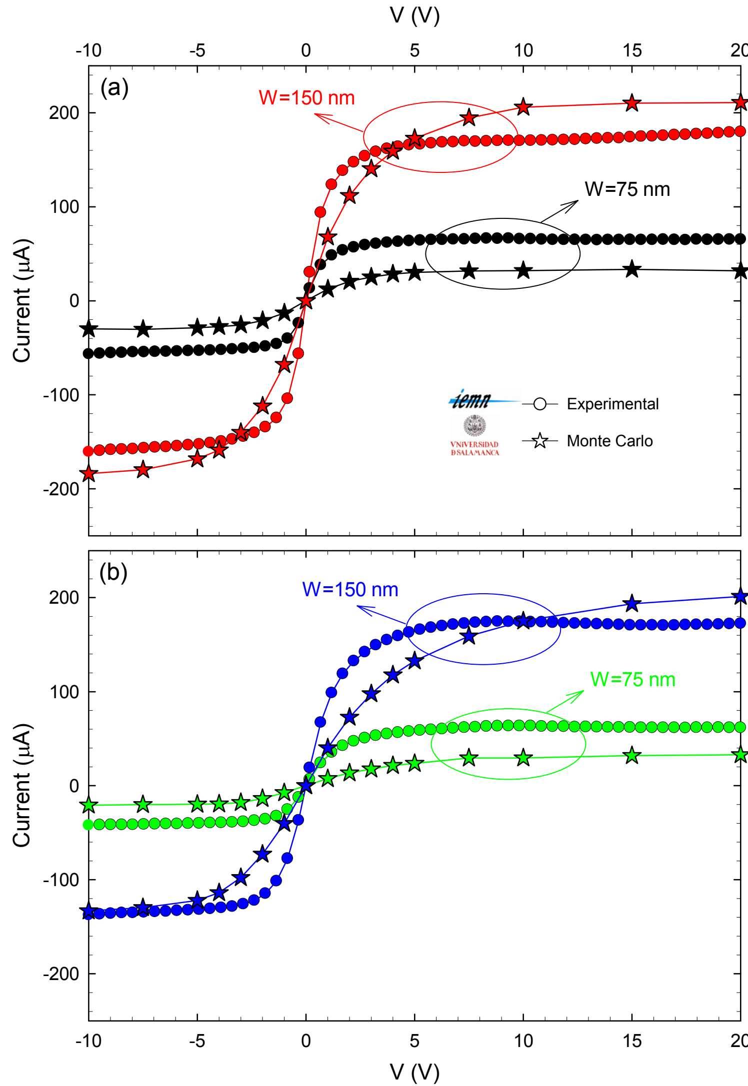

Figure 32. Comparison between experimental and simulated *I-V* curves of SSDs with channel length (a) 1 µm and (b) 2 µm (W_V=100 nm, W_H=50 nm, C=400 nm), and the indicated channel widths. $N_{Db}=1\times10^{17}$ cm^{-3} and $n_s=8\times10^{12}$ cm^{-2}.

Remarkably, once the *I-V* curves were satisfactorily reproduced, the current sequences calculated with the self-consistent model exhibited no oscillations.

III.3.d. Study of several quantities

In order to understand the effect of the self-consistent charge model, Figure 33(a) shows the profiles of the surface charge at equilibrium (or, equivalently, theoretical induced depletion W_d) for an SSD with W=75 nm and also with W=150 nm, both with L=1 µm. It can be observed that the profiles are non-homogeneous. Values of W_d about 25-30 nm are obtained, very close to those extracted from the experimental measurements, thus supporting the physical consistency of this model. The evolution of the profiles with the applied voltage, reported in Figure 33(b) and exhibiting a strong dependence on both the applied voltage and the position, explains the saturation of the current for voltages lower than in the case of using the constant surface charge model, and the lower value reached by the current.

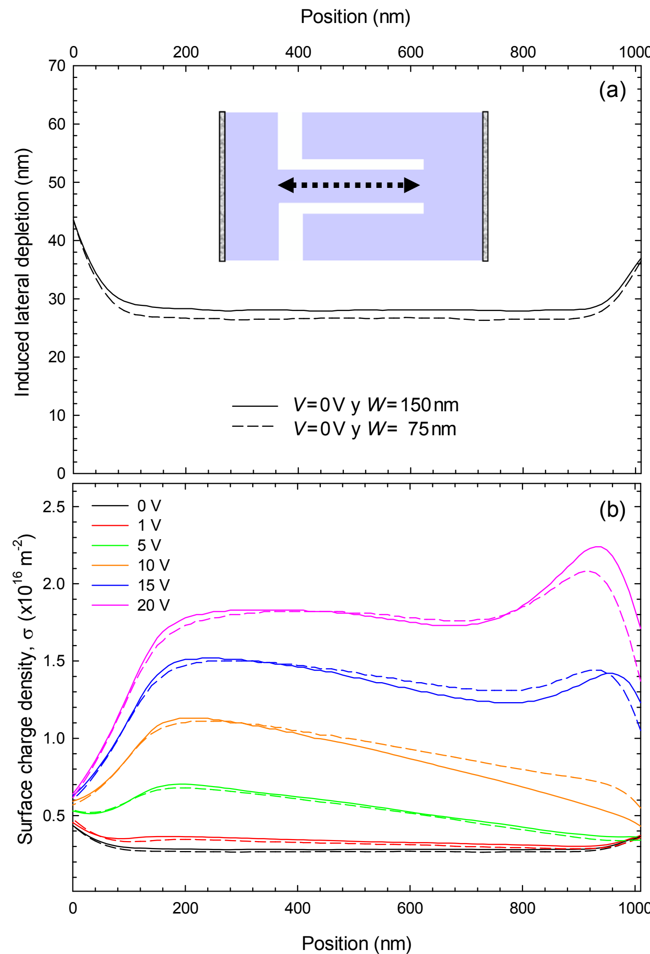

Figure 33. (a) Profiles of the induced lateral depletion in the channel by the surface charge in equilibrium conditions and (b) profiles of the surface charge for several applied voltages, for SSDs with L=1 µm and W=150 nm (solid lines) and W=75 nm (dashed lines).

It is really interesting and very illustrative to check the differences in the potential and electron concentration 2D maps between the two simulation models. Within the constant surface charge model the voltage applied to the anode contact V_{bias} practically reaches the sidewalls of the trenches surrounding the channel [Figure 34(a)], thus acting similarly to the gate voltage in a field effect transistor. This means that by increasing V_{bias} the carrier concentration in the channel should be higher, giving rise to an enhanced current. In fact, the carrier concentration is very high in the proximities of the horizontal trenches [Figure 34(c)]. Only for very high voltages a trend to saturation is observed due to electron velocity saturation effects in GaN. However, in the case of the self-consistent model the potential map is strongly affected by the surface charges [Figure 34(b)]. The potential at the boundaries of the trenches is not V_{bias} anymore. It gradually diminishes when moving far from the anode, provoking a significant decrease of the concentration of carriers close to the trenches [Figure 34(d)]. For higher V_{bias} the carrier concentration increases, and the value of the surface charge also rises [Figure 33(b)] due to the presence of more electrons in the proximity of the sidewalls of the channel, especially near the anode, where isotropic intervalley scattering takes place. In this framework the flux of current takes place mainly in the central part of the channel [Figure 34(d)]. The final result is that the influence of an increase of V_{bias} is relatively compensated by an enhanced σ, and the saturation regime is reached earlier, for much lower values of V_{bias} than within the constant surface charge model.

The role played by the charges present at the etched surfaces was known to be important in the behavior of the SSDs,[75] but these results show an unexpectedly strong influence, mainly due to the high applied voltages (much higher than in previously fabricated GaAs- or InGaAs-based SSDs). Indeed, the geometry of the first fabrication batch of diodes was designed with narrow channels (75 and 150 nm) expecting to have an electron concentration in the channel high enough for the onset of oscillations (relying on the results obtained with the constant surface charge model shown in the previous section). However, unfortunately both experimental measurements (S parameters up to 325 GHz) and MC simulations with the self-consistent model exhibited no oscillations due to an insufficient electron density in the channel. Thus, new design rules for the second run were proposed in order to achieve the onset of Gunn oscillations.

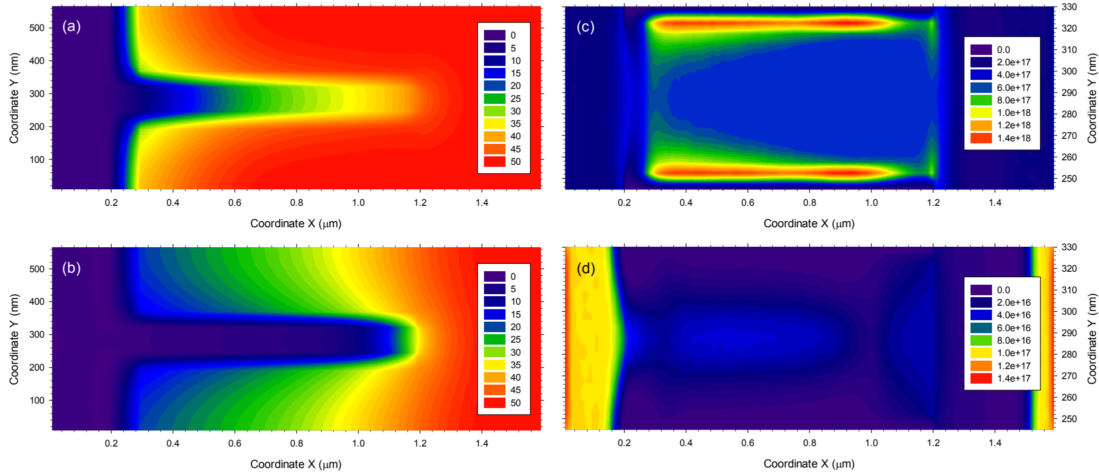

Figure 34. Two-dimensional maps (averaged in time) for the electric potential (units of V) for a diode with L=1 µm, W=75 nm and 50 V, using (a) the constant surface charge model (N_{Db}=2×10^{17} cm^{-3} and σ = 0.2×10^{12} cm^{-2}) and (b) the self-consistent one (N_{Db}=1×10^{17} cm^{-3}). In (c) and (d) the corresponding electron concentration (in units of cm^{-3}) are shown. In all the cases W_V=100 nm, W_H=50 nm and C=400 nm.

III.4. New design strategies and fabrication of Run 2

III.4.a. Indications with the constant surface charge model

Since the problem for the onset of the oscillations is the low carrier concentration present in the channel, we have first explored (in a fast way) with the constant surface charge model several geometries and combinations of SSD parameters (results not reported here) and the following conclusions have been found: (i) if the channel is totally depleted at equilibrium because of the high value of the surface charges, higher applied voltages are needed for the oscillations to appear, (ii) by increasing the width of the channel oscillations appear for lower voltages, and (iii) when increasing the background doping the onset of oscillations is also promoted.

III.4.b. Indications with the self-consistent surface charge model

With the self-consistent surface charge model, much more demanding from a computational point of view, two alternative geometries have been explored by simulations, both oriented to achieve higher electron concentration in the channel and avoid charge accumulation at its anode end. One is the use wider channels and the other the design of diodes with leaned horizontal trenches, leading to what we

call V-shape SSDs in contrast to the standard topology named square diode [Figure 35].

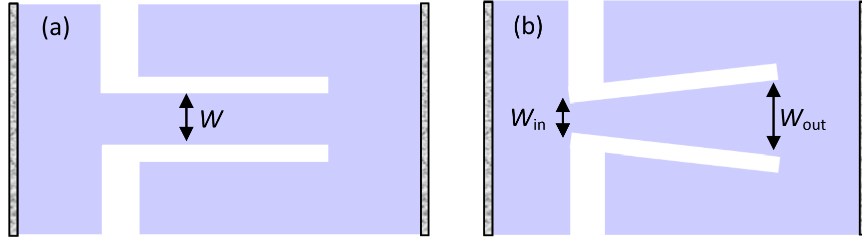

Figure 35. Geometry of the simulates diodes: (a) with the standard square shape and width W, and (b) with a V-shape geometry, W_{in} and W_{out} being the widths at the entrance and exit of the diode channel.

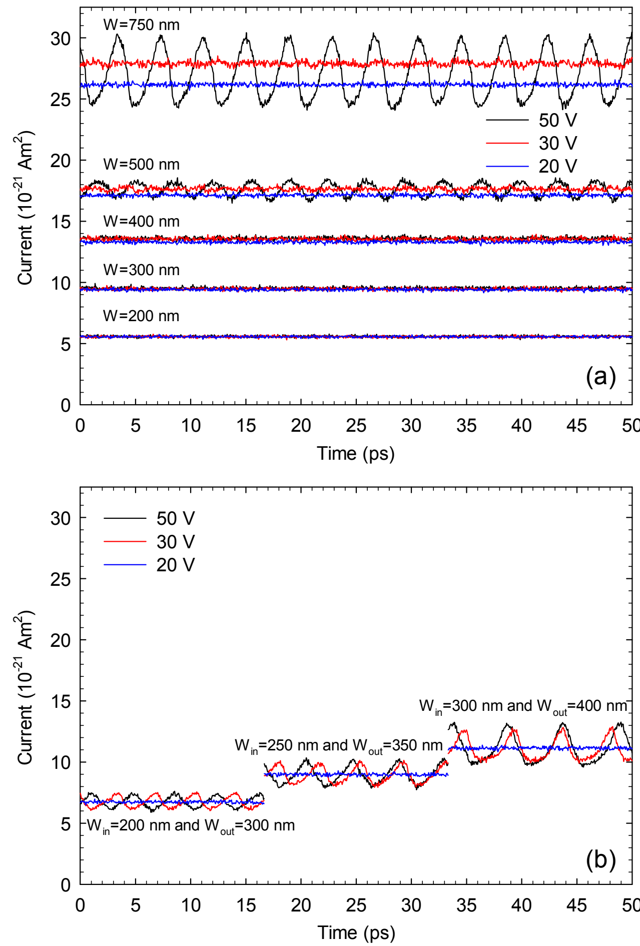

Figure 36. MC simulated current sequences for diodes with (a) square shape and (b) V-shape, and applied voltages of 20, 30 and 50 V. In all cases L=1 μm, W_V=100 nm, W_H=50 nm and C=400 nm. The value used for the virtual doping is $N_{Db}=5\times10^{17}$ cm^{-3}.

As concerns wider channels (always keeping a channel length of 1 μm), see Figure 36(a), current oscillations only appear $W > 500$ nm, with threshold voltages of about 40-50 V and frequencies around 300 GHz. Using the V-shape topology [see Figure 36(b)] we observe, for example, that for a diode with 200 nm of channel

width at the entrance (W_{in}) and 300 nm at the exit (W_{out}), clear oscillations are achieved already from 30 V. This will lead to higher efficiency values as compared with wider square diodes, since the DC current level is lower. MC microscopic results are able to explain the origin of this behavior in terms of the strong influence of the surface charge, especially at the channel exit, that is overcome by the additional opening in the V-shape diodes. Moreover, with these new designs the electric field at the entrance is high enough (thanks to the lower width) for the Gunn domains to be created.

A detailed spectral analysis of the current sequences using the FFT (Fast Fourier Transform) shows that for wider square channels the amplitude of the peaks in the spectra is noticeably larger (and also several harmonics even at 1.2 THz appear) although the frequencies are a bit lower. Also, the oscillation frequency slightly decreases with the applied bias. For the V-shape diodes, frequencies of hundreds of GHz appear, in this case from lower applied voltages than for the square diodes, thus confirming that this geometry favors the onset of the oscillations. The results for diodes with the same entry width but different exit widths indicate that there is an optimal ratio W_{out}/W_{in}, leading to an opening angle around 5-10º, for achieving maximum amplitude of the peaks in the spectra.

III.4.c. Experimental measurements

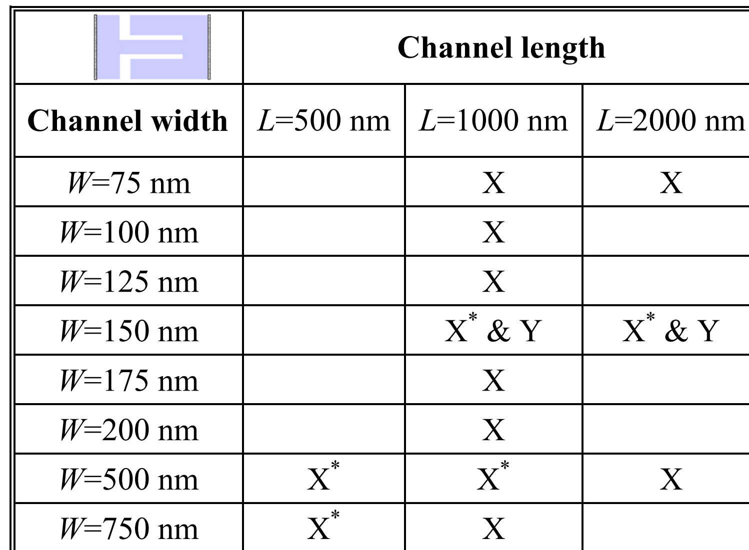

	Channel length		
Channel width	L=500 nm	L=1000 nm	L=2000 nm
W=75 nm		X	X
W=100 nm		X	
W=125 nm		X	
W=150 nm		X^* & Y	X^* & Y
W=175 nm		X	
W=200 nm		X	
W=500 nm	X^*	X^*	X
W=750 nm	X^*	X	

Table 2. Geometry of the fabricated square diodes. The symbol X^* stands for the devices fabricated both with trenches of W_H=100 nm, W_V=50 nm and of W_H=200 nm, W_V=100 nm. The symbol X means that only trench widths of W_H=100 nm, W_V=50 nm are used. The symbol Y means that the geometry is also fabricated with an integrated antenna.

In parallel with the simulation work the second run of devices started to be fabricated. In particular, 138 functional square SSDs with coplanar waveguide access were fabricated.

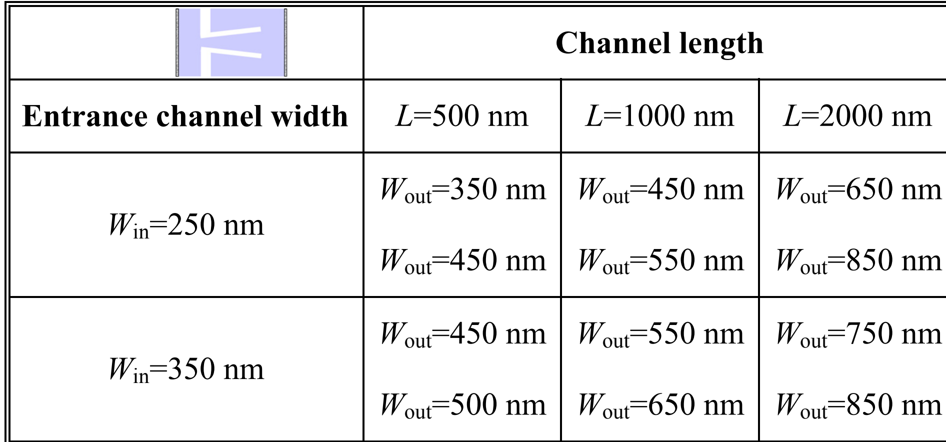	**Channel length**		
Entrance channel width	L=500 nm	L=1000 nm	L=2000 nm
W_{in}=250 nm	W_{out}=350 nm W_{out}=450 nm	W_{out}=450 nm W_{out}=550 nm	W_{out}=650 nm W_{out}=850 nm
W_{in}=350 nm	W_{out}=450 nm W_{out}=500 nm	W_{out}=550 nm W_{out}=650 nm	W_{out}=750 nm W_{out}=850 nm

Table 3. Geometry of the fabricated V-shape diodes. In all cases W_H=100 nm and W_V=50 nm. The case with W_{in}=250 nm, W_{out}=650 nm and L=2000 nm is also fabricated with an integrated antenna.

Table 2 and Table 3 summarize the dimensions of the fabricated devices. Note that also narrow channel devices were designed for detection studies within the project.[140] In this second run some of the devices (indicated in the tables) were integrated with bow-tie antennas (with length of 300 μm, operative up to a few 100's of GHz) in order to perform free space measurements of detection (narrow SSDs) and emission (wide SSDs). Each bow-tie antenna contains 64 SSDs and arrays of 6 and 8 antennas have been put together. These designs with many devices in parallel have been made, on the emission side, in order to increase the generated power and, on the detection side, to decrease the global impedance and the noise equivalent power NEP of the detectors.[140]

At this stage I spent three months in Lille performing the DC measurements of all of these diodes, the conclusions being:

i. The I-V curves exhibit nearly the same current levels as in the first run, showing a good reproducibility of the technological process on GaN.

ii. The expected linear increase in the current level versus the number of SSDs is obtained, the current level mainly depending on the channel width, W, and not on the channel length, L (that just affects the slope before saturation).

iii. The depletion width associated with the surface charges is about 35 nm (17.5 nm at each side of the channel) for low voltages, and decreases when increasing the bias in agreement with the MC simulations.

iv. For the V-shape designs the current level is primarily fixed by the width at the entrance of the channel.

After the DC measurements the devices were bounded and mounted on a PCB board for free-space emission experiments. First, a pyrometer detector calibrated at 300 GHz was used. We had detected few tens of mV at the lock-in, but this signal was still present at low bias (< 10 V), at a voltage at which no oscillation should occur. By putting an IR filter we have identified that such a signal was infrared emission due to the high temperature of the devices. Further measurements were performed with a Schottky barrier detector, operational at 220-325 GHz with sensitivity of 1 kV/W, but strong heating problems appeared. Several devices were burnt out for biasing conditions between 20 and 30 V when reaching current levels of 150-370 mA.

III.5. Simulations and experimental measurements in Run 3

III.5.a. Design and fabrication

After measurements on Run 2 devices, and taking into account the results of MC simulations and possible technological improvements to be made a new mask design was carried out.

The main design rules in Run 3 following MC indications were:

i. Give priority both to wider square SSDs and, especially, to V-shape SSDs.

ii. Fabricate shorter channels in order to increase the expected oscillation frequency.

iii. Limit the number of channels in parallel and increase the separation between them. Only one antenna is integrated in the SSD arrays, and its distance between anode and cathode was reduced.

The work presented in the following sections corresponds to my most recent contribution to the project, performed the last months before writing this dissertation.

III.5.b. Simulations and experimental measurements

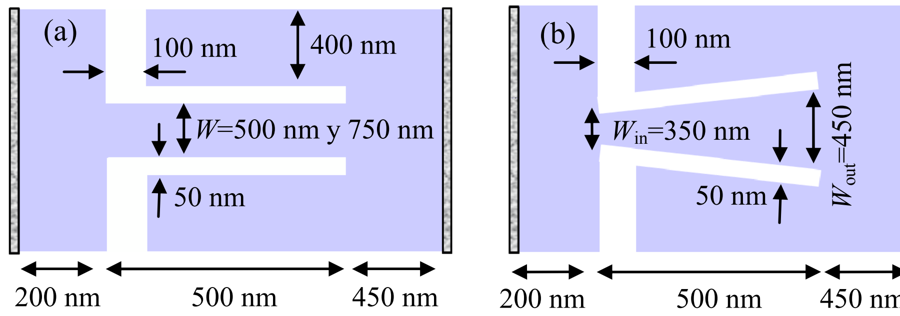

Figure 37. Geometry of the simulated devices for comparison with Run 3.

Three of the GaN SSDs fabricated in this run have been simulated, all of them with a short channel length, L=500 nm. Two are square diodes with channel width of 500 and 750 nm and the third is a V-shape diode with 350 nm width at the entrance and 450 nm at the exit of the channel. The devices are sketched in Figure 37. A satisfactory agreement between the simulated *I-V* curves and the measurements done at the IEMN has been achieved, as observed in Figure 38(a)-(c). Even if the saturation level is well reproduced, work is still to be done to improve the disagreement in the low bias region. *I-V* characteristics do not show a strong rectifying behavior because the channel widths are large, but since they are designed to produce THz emission this is not a problem. It is to be noted that both Run 2 and Run 3 provide nearly the same *I-V* curves for devices with identical topology, thus demonstrating the maturity of the fabrication process.

Once the *I-V* curves are fitted, the presence of oscillations in the diodes is analyzed. Figure 38(d)-(f) shows the time sequences of the current in the three diodes for three increasing applied voltages. As observed, the change in the width from 500 to 750 nm significantly enhances the amplitude of the oscillations in the square diode, but the consumed DC power is also higher. The V-shape is the most favorable geometry for the onset of the oscillations, since they appear for lower applied voltages and with lower current levels. This means that less DC power will be dissipated by the V-shape devices and higher efficiencies can be achieved. The oscillation frequency is about 370 GHz in the three structures, the highest value achieved so far in the simulated diodes, as corresponds to their short length, 500 nm. This fact confirms that the oscillation frequency can be enhanced by shortening the diodes as far as they are correctly designed.

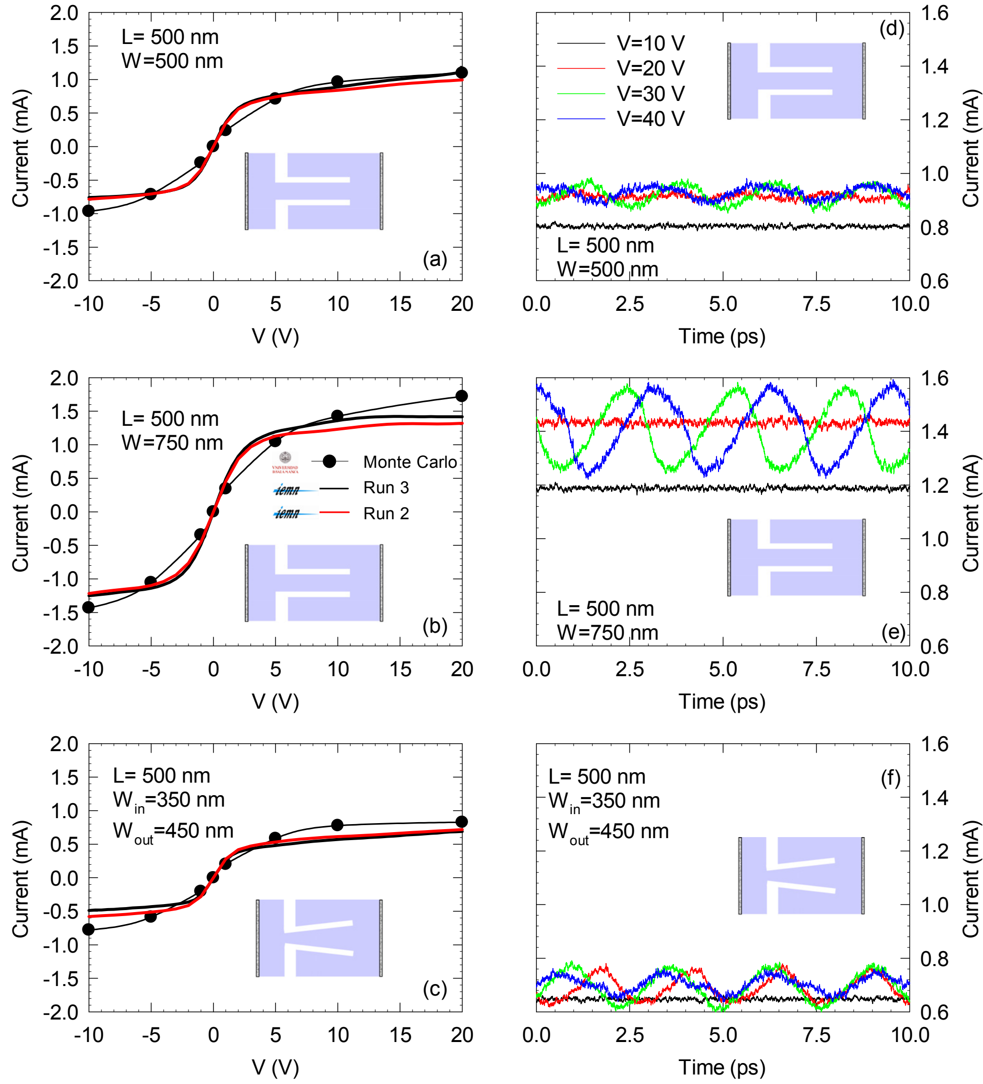

Figure 38. (a)-(c) Comparison between experimental *I-V* curves of Run 2 and Run 3 and MC simulations. (d)-(f) MC simulations of current sequences for different applied voltages. The value used for the virtual doping is N_{Db}=5×10^{17} cm^{-3} and for the sheet carrier density n_s=6×10^{12} cm^{-2}.

To test the possible influence of device heating on the onset of oscillations, a square diode with a channel width of 750 nm is simulated considering an operating temperature of 500 K (Figure 39). Oscillations are still present but the threshold voltage for their onset is higher, and their frequency lower (about 290 GHz), as expected from the lower saturation velocity of GaN at 500 K.

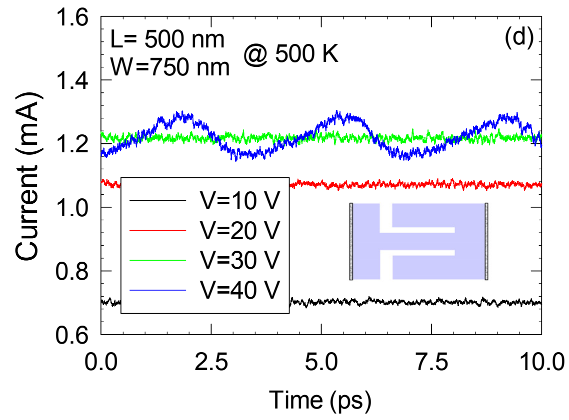

Figure 39. Simulated current sequences at 500 K for a square diode with W=750 nm.

On the other hand, in order to avoid an excessive device heating when doing the experimental measurements, a set-up for pulse measurements will be developed in order to confirm the presence of emission in Run 3 devices.

IV. CORRELATION BETWEEN LOW-FREQUENCY NOISE AND HIGH-FREQUENCY OSCILLATIONS

It is still quite tricky to carry out experimental measurements at hundreds of GHz. For that reason, alternative methods of analysis become crucial into the field of terahertz or sub-THz electronic devices, in particular to detect the presence of oscillations in this frequency range. A first possible indicator is related to the kinks that sometimes appear in the *I-V* curves for applied voltages at which the onset of instabilities take place, indicating the transition from a passive- to a generation-state. However, in the cases studied in this work, these kinks are not very clear in the *I-V* curves of the OPTTR (Optical Phonon Transit Time Resonance) [Figure 12] or even inexistent in the *I-V* curves of the SSDs (Self-Switching Diodes), though clear oscillations are observed. Another prediction method already suggested by other authors[141,142] consists in the use the low-frequency noise in the current $S_I(0)$ as indicator of the onset of oscillations, since it exhibits a significant enhancement for voltages approaching the threshold for their appearance. The aim of this chapter is to check, by means of Monte Carlo (MC) simulations, if this behavior takes place both in the n^+nn^+ diodes and the SSDs based on gallium nitride (GaN) object of study in this thesis. These are promising devices for THz generation and a lot of difficulties have been found at the time of measuring the emission. Thus, we analyze the possibility of indirectly detecting the presence of current oscillations by the enhancement of low-frequency noise.

First we will present the results concerning the SSDs, extensively published in Ref. 143, and then those related to the OPTTR mechanism.

Let us remember at this point that to perform a frequency analysis of electrical fluctuations and to detect the presence of current oscillations, the time-domain current sequences obtained from the MC simulations are Fourier transformed (once subtracted the average DC value), the resulting magnitude being squared to obtain the current noise spectral density $S_I(f)$ in the frequency domain. The current-noise calculated at zero frequency $S_I(0)$, corresponding to the noise measured in experiments in the plateau beyond 1/*f* and generation-recombination noise, will be used as the indicator for the occurrence of oscillations.

IV.1. Low frequency noise in SSDs

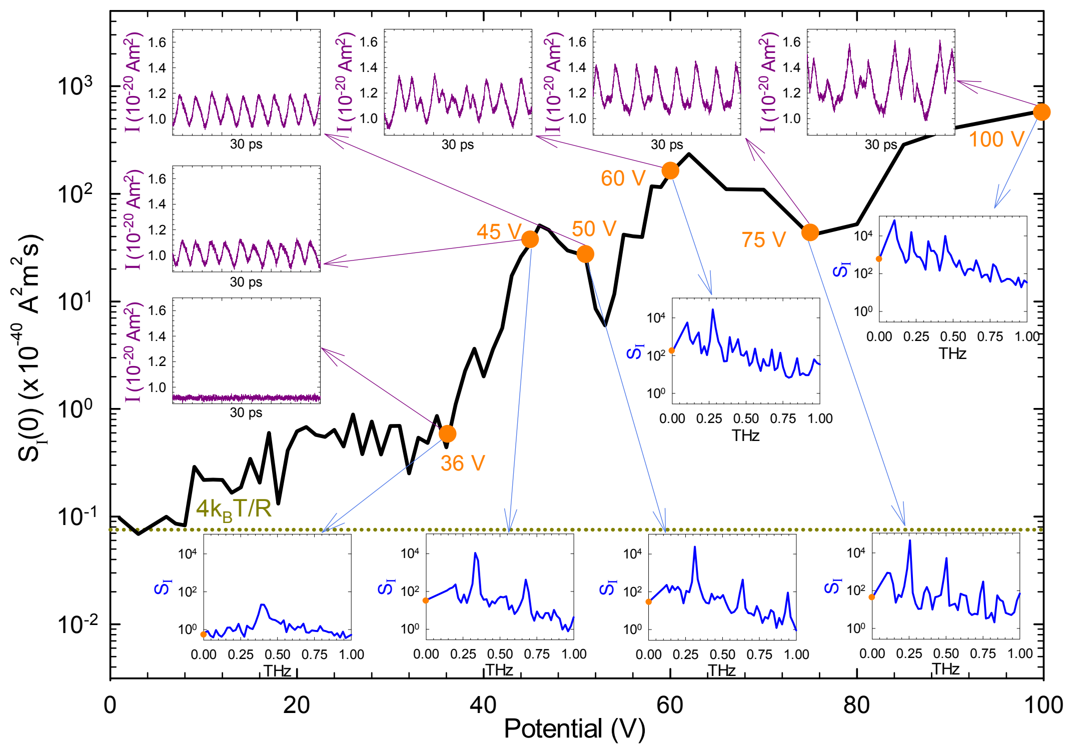

Figure 40. Low-frequency value of the current spectral density as a function of the bias for SSD1, where $\sigma = -0.25\times10^{12}$ cm^{-2}. The insets show current sequences and the corresponding spectral densities for several significant applied voltages.

For the calculations, a square SSD with the following geometry will be considered: L=1 μm, W=80 nm, W_V=100 nm, W_H=50 nm, and C= 400 nm [see Figure 7(b)]. The virtual doping is $N_{Db} = 2\times10^{17}$ cm^{-3}. Three different values of the surface charge density are used within the constant surface charge model. A large value of σ contributes to deplete the channel and higher voltages are necessary for obtaining oscillations. In the first simulated diode (SSD1) we have set

$\sigma = -0.25\times10^{12}$ cm^{-2}, in the second one (SSD2) $\sigma = -1.0\times10^{12}$ cm^{-2} and $\sigma = -1.5\times10^{12}$ cm^{-2} in the last one (SSD3).

Figure 40 shows the low-frequency current noise as a function of the applied voltage for the first diode, the one with the lower value considered for the surface charge density, i.e. $\sigma = -0.25\times10^{12}$ cm^{-2}. Current sequences and noise spectra are also plotted as insets in order to get more information about what happens in the diode for several voltages at which $S_I(0)$ exhibits significant variations. Both noise and current values reported in the results have been normalized in such a way that just multiplying them by the value of the sheet electron density in the channel of a real device, S_I and I are obtained in units of A^{2}s and A, respectively. We note that at such particular voltages there are no kinks in the *I-V* curve, shown in Figure 41(a). As can be observed, the threshold for the onset of Gunn oscillations is about 36 V. Below this voltage, starting from the Nyquist value at equilibrium, the noise exhibits a slight increase with the bias due to electron heating. For voltages higher than 36 V, a remarkable enhancement of the low-frequency noise is detected, in parallel to the transition from a passive to a generation state as evidenced by the current sequence and its corresponding spectral density at 45 V. Once the oscillations are well established (V > 45 V), $S_I(0)$ decreases and then, at around 53 V, it increases again because of the onset of further frequency components, as observed for 60 V. For higher voltages we find once more the previously explained behavior, i.e. a drop in the noise up to 75 V due to the presence of clear oscillations followed by another rise according to the incorporation of more harmonics, as occurs at 100 V.

In order to confirm that the enhancement of the low-frequency noise is certainly due to the onset of current oscillations and further spectral components, simulation results for the two other SSDs are presented in Figure 41. A higher value of σ leads to a stronger channel depletion that makes necessary higher voltages to achieve, first, current conduction through the diode, and then Gunn oscillations, as shown in Figure 41(a). In SSD2 oscillations are more difficult to be obtained than in SSD1, being necessary the application of a voltage around 80 V, while for SSD3 the effective width of the channel is not enough to achieve current oscillations even at 100 V. In fact, the current level is much lower than in the other diodes.

With regard to the low-frequency noise [see Figure 41(b)], the curve corresponding to SSD2 exhibits a more or less constant value up to 80 V (with a

slight increase due to electron heating) and then rises considerably, coinciding with the onset of oscillations at that voltage. For a lower value of σ, which is the case of SSD1 presented before, such a bump takes place at lower bias, at 36 V, while for a higher value of σ, as occurs for SSD3, $S_I(0)$ remains practically constant since no oscillation is achieved.

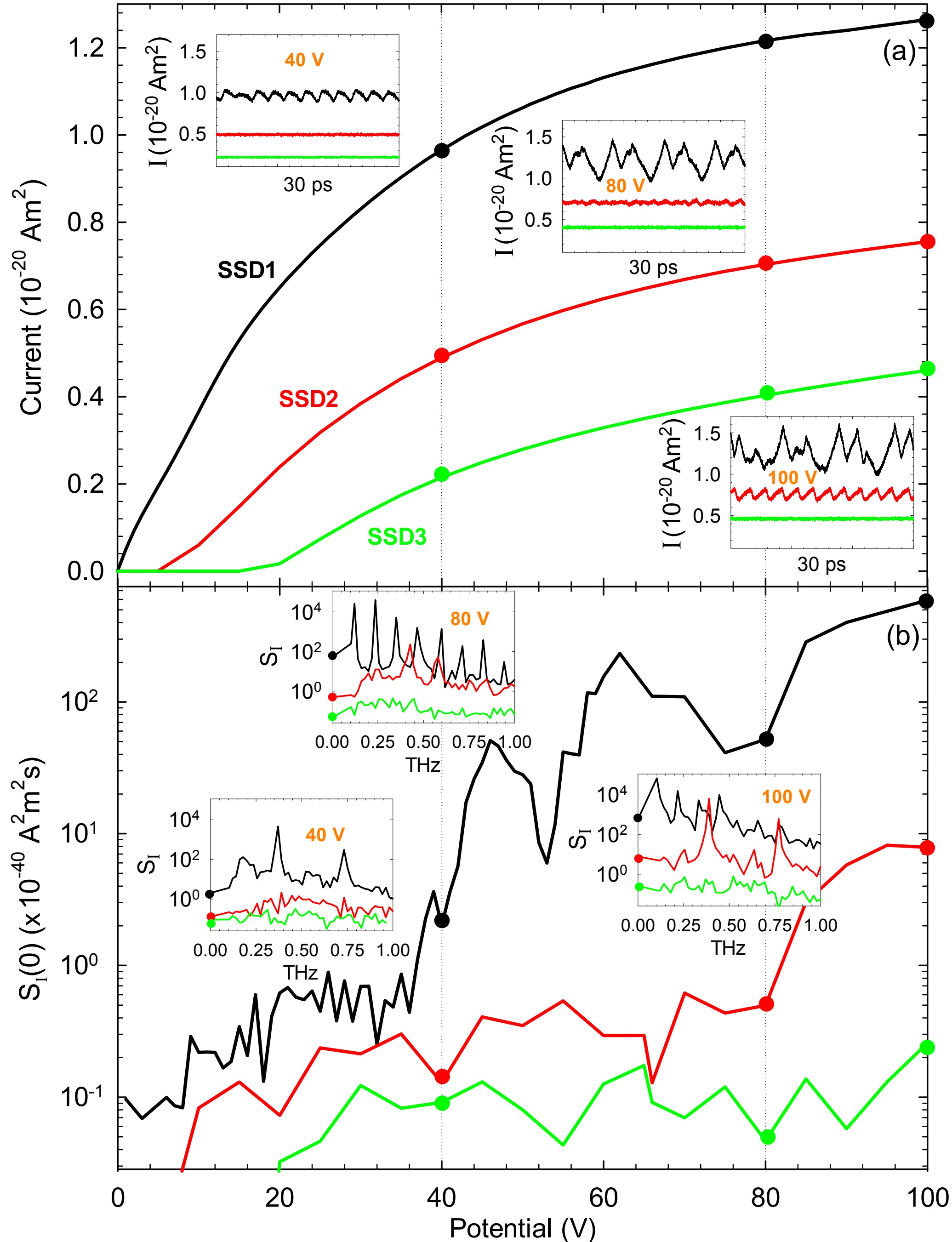

Figure 41. (a) *I*-*V* curves and (b) low-frequency value of the current spectral density for SSD1 (same as in Figure 40), that has $\sigma = -0.25\times10^{12}$ cm^{-2}, and two more diodes, SSD2 and SSD3, with $\sigma = -1.0\times10^{12}$ cm^{-2} and $\sigma = -1.5\times10^{12}$ cm^{-2}, respectively. The insets in (a) show current sequences for 40, 80 and 100 V and in (b) the corresponding spectra.

IV.2. Low frequency noise in the OPTTR

In the case of the OPTTR mechanism the so called reference diode in Chapter II (Figure 12) will be considered, and the influence of the temperature on the results when operating at 15, 40 and 150 K will be analyzed. In Figure 42 we show the low-frequency value of the current spectral density as a function of the bias for the three simulated temperatures. The plotted values of the spectral density have been normalized in such a way that its absolute value in A^2s can be obtained just multiplying by the non-simulated dimension of the n^+nn^+ diodes.

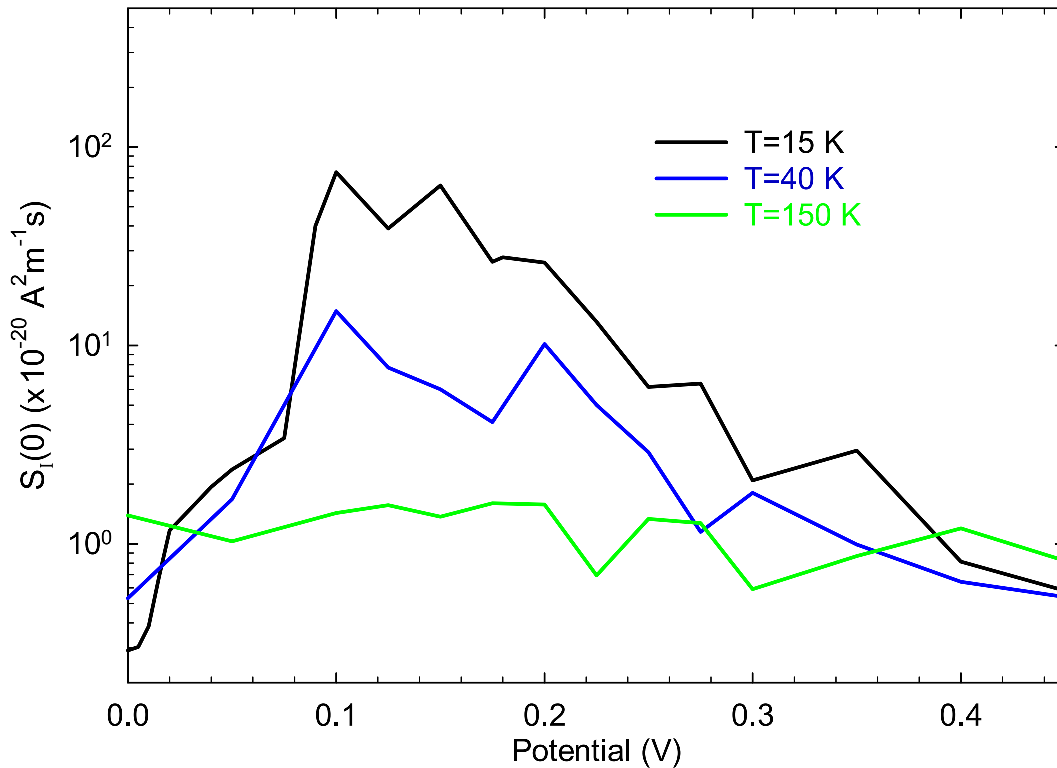

Figure 42. Low-frequency value of the current spectral density as a function of the bias for the GaN n^+nn^+ diode of Figure 12 at 15 K, and also at 40 and 150 K.

At 15 K, and even at 40 K (but in a less pronounced way), a remarkable enhancement of the low-frequency noise is detected at around 0.1 V, due to the onset of current oscillations when reaching the optical phonon energy. Contrary to what happens in the SSDs, when increasing the applied voltage $S_I(0)$ decreases since the oscillation conditions are not fulfilled, leading to the disappearance of the oscillations. Finally, for the higher value of temperature, 150 K, $S_I(0)$ remains practically constant at the thermal equilibrium value since no oscillation is achieved.

Once confirmed by MC simulations the possibility of indirectly detecting the presence of current oscillations at high frequencies by the enhancement of low-frequency noise, it is time to be exploited from the experimental point of view. So our colleagues at the IEMN (*Institut d'Electronique, de Microélectronique et de Nanotechnologie*), where the GaN SSDs under study in the third chapter are fabricated and characterized, are expected to carry out noise measurements in this context to overcome in some way the difficulties encountered so far to detect emission in the sub-THz frequency range.

CONCLUSIONS

In this dissertation two candidates for the generation of THz signals within the approach based on solid-state devices have been analyzed: (i) coherent plasma oscillations in micrometric GaN n^+nn^+ diodes induced by optical phonon emission (OPTTR, Optical Phonon Transit Time Resonance) and (ii) Gunn oscillations in nanometric Self-Switching Diodes (SSDs) based on GaN. Monte Carlo (MC) simulations and measurements in devices fabricated at IEMN (*Institut d'Electronique, de Microélectronique et de Nanotechnologie*, Lille, France) are combined in the analysis.

The main conclusions are as follows:

- **OPTTR in GaN n^+nn^+ diodes**

  - OPTTR originates charge accumulations along the n region of the diodes in the zones where optical phonon emissions (OPEs) take place, which tend to oscillate at its plasma frequency f_p.

  - When f_p is close to the inverse of the time interval between OPEs, f_E, and charge accumulations are separated enough from each other (to guarantee the synchronization of the OPEs along the diode through the feedback provided by the self-consistent electric field), i.e. $l_0 >> \lambda_D$, significant current oscillations of frequency f_E appear.

- The profiles of various magnitudes like OPE rate or electric field show the associated inhomogeneities in time and space.

- When temperature is raised the coherence is degraded mainly because of the growing influence of other scattering mechanisms.
- By increasing the length of the *n* region, current oscillations take place in a wider bias range, but without any improvement of the maximum frequency of oscillation.
- A frequency enhancement can be achieved by increasing the doping of the diode; for $n=10^{16}$ cm^{-3} and $n^{+}=10^{18}$ cm^{-3}, current oscillations with frequencies above 1 THz are obtained in 1-2 μm diodes.

- **Gunn oscillations in GaN self-switching diodes**

Several properties of GaN, like its high threshold and breakdown fields, and high electron saturation velocity, makes it a promising material to fabricate devices exploiting Gunn effect to obtain high power and high frequency signals, approaching the THz range. The simple geometry of SSDs, planar devices where L-shaped etched trenches break the symmetry of the channel, is favorable (combined with the above properties of GaN) for the emission of THz signals at room temperature.

Previously to any fabrication run, using the simple (and fast) **constant surface charge MC model,** simulations of different devices were performed to confirm the principle of operation of the diodes and the dependence of their performance on several characteristic parameters (geometrical, physical and of the MC model). The main findings were:

- 1 μm channel-length SSDs exhibit current oscillations at room temperature for voltages above 30 V at frequencies around 300 GHz.
- The analysis of the *I-V* curves and the current sequences shows that:
    - The oscillation frequency essentially scales with the channel length *L*.
    - Even if of lower amplitude and frequency, Gunn oscillations are still present at 500 K.
    - The increase of the surface charge σ induces stronger channel depletion, thus leading to a smaller current level and lower amplitude and frequency of the oscillations, which even disappear for the higher σ.

- As the background doping N_{Db} increases, Gunn oscillations are reinforced.

- The DC to AC conversion efficiency exhibits several bands of AC generation, with a usual maximum value between 0.1 and 0.5 %, at the fundamental frequency of the Gunn effect and also at around double frequency.

A first batch of diodes (Run 1), a challenge in GaN technology because of their small dimensions, was successfully fabricated. However, no oscillation was found due to the strong and unexpected influence of surface charge, which was identified by means of MC simulations. A **self-consistent charge model** was necessary to reproduce the experimental *I-V* curves. Once fitted, the simulations showed no oscillations, like happening in measurements.

- The new model evidenced that the surface charge density along the boundary of the trenches is strongly non-homogeneous and voltage dependent. The depletion induced by the surface charge reduces the carrier concentration in the channel and inhibits the formation of Gunn domains.

- MC simulations indicate that wider channels where carrier concentration is larger and improved geometries to counteract the influence of surface charge, as the so called V-shape diodes, must be used in next fabrication runs in order to achieve the oscillations.

- A detailed spectral analysis of the simulated current sequences in the newly designed diodes shows that:

  - For wider square channels the amplitude of the peaks in the spectra is noticeably larger although the frequencies are a bit lower (but more harmonics reaching even 1.2 THz appear).

  - For the V-shape diodes, frequencies of hundreds of GHz are achieved, in this case from applied voltages lower than for the square diodes, thus confirming that this geometry favors the onset of the oscillations and can lead to higher efficiencies. Moreover, there is an optimal ratio W_{out}/W_{in}, leading to an opening angle around 5-10º, for achieving maximum amplitude of the peaks in the spectra.

  - The oscillation frequency slightly decreases with the applied bias.

In parallel with the simulation work, the second run of devices (Run 2) was fabricated. Some of the diodes were integrated with bow-tie antennas and many devices were designed with a very narrow channel, mainly oriented for detection studies.

- The DC measurements of all of these diodes, performed by me during a three-month research stay at IEMN, confirmed the expected dependence of the I-V curves on the geometrical parameters and showed a good reproducibility of the technological process on GaN. However, neither the simulation results nor the experimental free-space measurements (where heating problems were met) found Gunn oscillations.

The third fabrication run (Run 3) followed the design rules defined from the results of MC simulations, giving priority both to wider square SSDs and, especially, to V-shape SSDs. Moreover, the number of channels in parallel was limited and the separation between them increased to avoid the heating problems found in previous measurements.

- MC simulations nicely reproduce the *I-V* curves of the new devices and predict current oscillations (of frequency about 370 GHz according to a shorter channel length L=500 nm) that are still to be confirmed by experimental experiences with an especially designed pulse measurement set-up.

- **Correlation between low-frequency noise and high-frequency oscillations**

Since experimental techniques at frequencies of hundreds of GHz are still rather tricky, alternative procedures to detect the presence of the THz or sub-THz oscillations predicted by simulations are needed. The low-frequency noise spectral density is shown to be a good indicator to this end in the two phenomena (and related devices) analyzed in this work.

- In the case of SSDs, the spectral densities calculated from MC current sequences exhibit a clear enhancement of the low-frequency noise just for voltages corresponding to the onset of current oscillations and also when higher harmonic components emerge.

- A similar behavior is found in the case of the OPTTR mechanism, i.e. a remarkable enhancement of the low-frequency noise is detected due to the onset of current oscillations when the applied voltage exceeds the optical phonon energy, what happens at around 0.1 V. Nevertheless, in this case a further increase of the bias finally leads to a decrease of $S_I(0)$ since the oscillations tend to disappear.

- The measurement of $S_I(0)$ could be useful to identify the presence of oscillations in the GaN n^+nn^+ diodes and SSDs analyzed here, and thus circumvent the well-known difficulties of experimental measurements in this frequency range.

This work has been performed under the support of a PhD Grant of **Formación de Personal Investigador** from the Spanish Ministerio de Ciencia e Innovación (BES-2008-003434).

It corresponds to research activities carried out by the **Grupo de Investigación en Dispositivos Semiconductores de la Universidad de Salamanca** in the framework of the following **research projects**:

- Modelización de HEMTs avanzados para aplicaciones de alta frecuencia: nuevos materiales, estructuras y conceptos (TEC2007-61259/MIC). Ministerio de Educación y Ciencia - Dirección General de Investigación.
- Dispositivos semiconductores para aplicaciones en el rango de THz: nuevos materiales y arquitecturas (GR270). Junta de Castilla y León - Consejería de Educación - Grupos de Excelencia.
- Semiconductor nanodevices for room temperature THz emission and detection. ROOTHz (ICT-2009-243845). European Comission.
- Estudio de los fenómenos de ionización por impacto en dispositivos electrónicos avanzados de semiconductores III-V para aplicaciones en el rango de frecuencias milimétricas y submilimétricas (FS/18-2010). Fundación Memoria D. Samuel Solórzano Barruso.
- Diodos y transistores avanzados para generación, detección y procesado de señales milimétricas y submilimétricas (TEC2010-15413). Ministerio de Ciencia e Innovación - Dirección General de Investigación.
- Nanodispositivos semiconductores para la emisión y detección de radiación de THz a temperatura ambiente (SA183A12-1). Junta de Castilla y León - Consejería de Educación.

Part of the results collected in this dissertation have been published in the following **articles in scientific journals**:

- Íñiguez-de-la-Torre A., Mateos J. and González T., "Terahertz current oscillations assisted by optical phonon emission in GaN n^+nn^+ diodes: Monte Carlo simulations", *J. Appl. Phys.* **107**, 053707 (2010).

- Íñiguez-de-la-Torre A., Íñiguez-de-la-Torre I, Mateos J. and González T., "Correlation between low-frequency current-noise enhancement and high-frequency oscillations in GaN-based planar nanodiodes: A Monte Carlo study", *Appl. Phys. Lett.* **99**, 062109 (2011).
- Íñiguez-de-la-Torre A., Íñiguez-de-la-Torre I., Mateos J., González T., Sangaré P., Faucher M., Grimbert B., Brandli V., Ducournau G. and Gaquière C., "Searching for THz Gunn oscillations in GaN planar nanodiodes", *J. Appl. Phys.* **111**, 113705 (2012).
- Sangaré P., Ducournau G., Grimbert B., Brandli V., Faucher M., Gaquière C., Íñiguez-de-la-Torre A., Íñiguez-de-la-Torre I., Millithaler J. F., Mateos J. and González T., "Experimental Demonstration of Direct Terahertz Detection at Room-Temperature in AlGaN/GaN Asymmetric Nanochannels". *Nano Lett.* Manuscript submitted for publication (2012).

As well, part of the results have been presented in the following **communications to national and international conferences** and are collected in the corresponding **proceedings**:

- Íñiguez-de-la-Torre A., González T. and Mateos J., "Current oscillations excited by optical phonon emission in GaN n^+nn^+ diodes: Monte Carlo simulations", 16th International Conference on Electronic Dynamics in Semiconductors, Optoelectronics and Nanostructures (EDISON). Poster. Montpellier (France), August 2009. Published in *J. Phys.: Conf. Series* **193**, 012023 (2009).
- Íñiguez-de-la-Torre A., Mateos J. and González T., "OPTTR induced THz current oscillations in Monte Carlo simulated GaN diodes", Journées Nationales du Réseau Doctoral de Micro-électronique (JNRDM). Oral. Montpellier (France), June 2010.
- Íñiguez-de-la-Torre A., Mateos J. and González T. "OPTTR induced current oscillations in GaN diodes. Monte Carlo simulations", 8th Spanish Conference on Electron Devices (CDE). Poster. Palma de Mallorca (Spain), February 2011. Published in *IEEE Conference Publications*, DOI: 10.1109/SCED.2011.5744233.

- Íñiguez-de-la-Torre A., Mateos J., Íñiguez-de-la-Torre I. and González T. "Toward THz Gunn Oscillations in Planar GaN Nanodiodes", 8th Spanish Conference on Electron Devices (CDE). Invited Oral presentation. Palma de Mallorca (Spain), February 2011. Published in *IEEE Conference Publications*, DOI: 10.1109/SCED.2011.5744219.

- Gaquière C., Ducournau G., Sangaré P., Grimbert B., Faucher M., Íñiguez-de-la-Torre I., Íñiguez-de-la-Torre A., González T. and Mateos J. "Wide band gap self switching nanodevices for THz applications at room temperature", 41st European Microwave Conference (EuMC). Oral. Manchester (UK), October 2011. Published in *IEEE Conference Publications*, 1150 (2011).

- Íñiguez-de-la-Torre A., Mateos J., Íñiguez-de-la-Torre I. and González T. "Room Temperature THz Gunn Oscillations in GaN Nanodiodes", 20th Heterosctructure Technology (HeTECH). Oral. Villeneuve d'Ascq. Lille (France), November 2011.

- Gaquière C., Ducournau G., Sangaré P., Faucher M. ,Grimbert B., Íñiguez-de-la-Torre I., González T., Íñiguez-de-la-Torre A. and J. Mateos, "THz Applications at Room Temperature Based on Self Switch Diodes Using wide Bandgap Material", IEEE International Microwave Symposium (IMS), Oral, Montréal, Québec (Canada), June 2012.

- Mateos J., Millithaler J. F., Íñiguez-de-la-Torre I., Íñiguez-de-la-Torre A., Vasallo B. G., Pérez S., Sangaré P., Ducournau G., Gaquière C., Alimi Y., Zhang L., Rezazadeh A., Song A. M., Westlund A., Grahn J. and González T., "Room Temperature THz Detection and Emission with Semiconductor Nanodevices". Manuscript submitted to 9th Spanish Conference on Electron Devices (CDE), Valladolid (Spain), February 2013.

A three-month research stay (20/09/2011-20/12/2011) was performed at the IEMN (*Institut d'Electronique, de Microélectronique et de Nanotechnologie*) in Lille (France).

REFERENCES

[1]Bryant John H., *Heinrich Hertz, the beginning of microwaves: discovery of electromagnetic waves and opening of the electromagnetic spectrum by Heinrich Hertz in the years 1886-1892* (New York: Institute of Electrical and Electronics Engineers, 1988).

[2]Mueller E. R., "Terahertz Radiation: Applications and Sources", *The Industrial Physicist, American Institute of Physics* **9**, 27 (2003).

[3]Beard M. C., Turner G. M. and Schmuttenmaer C. A., "Progress toward two-dimensional biomedical imaging with THz spectroscopy", *Phys. Med. Biol.* **47**, 3841 (2002).

[4]Siegel P. H., "Terahertz Technology", *IEEE Trans. Microwave Theory and Tecnhiques* **50**, 910 (2002).

[5]Siegel P. H., "Terahertz Technology in Biology and Medicine", *IEEE Trans. Microwave Theory and Tecnhiques* **52**, 2438 (2004).

[6]Crowe T. W., Bishop W. L., Porterfield D. W., Hesler J. L. and Weikle R. M., "Opening the Terahertz Window With Integrated Diode Circuits", *IEEE J. Solid-State Circuits* **40**, 2104 (2005).

[7]Federici J. F., Schulkin B., Huang F., Gary D., Barat R., Oliveira F. and Zimdars D., "THz imaging and sensing for security applications-explosives, weapons and drugs", *Semicond. Sci. Technol.* **20**, S266 (2005).

[8]Shur M., "Terahertz technology: devices and applications", Proceedings of the 35th European Solid-State Device Research Conference (ESSDERC), *IEEE*, 13 (2005).

[9]Mann C., "Practical Challenges for the Commercialisation of Terahertz Electronics", *IEEE MTT-S Int. Microwave. Symp.*, 1705 (2007).

[10]Tonouchi M., "Cutting-edge terahertz technology", *Nature Photon.* **1**, 97 (2007).

[11]Kibis O. V., da Costa M. R. and Portnoi M. E., "Generation of Terahertz Radiation by Hot Electrons in Carbon Nanotubes", *Nano Lett.* **7**, 3414 (2007).

[12]Rangel N. L. and Seminario J. M., "Graphene Terahertz Generators for Molecular Circuits and Sensors", *J. Phys. Chem. A* **112**, 13699 (2008).

[13]Tsujimoto M., Minami H., Delfanazari K., Sawamura M., Nakayama R., Kitamura T., Yamamoto T., Kashiwagi T., Hattori T. and Kadowaki K., "Terahertz imaging system using high-T_c superconducting oscillations devices", *J. Appl. Phys.* **111**, 123111 (2012).

[14]Offranc O., "Composants pour la génération et la détection d'impulsions térahertz", *Tesis Doctoral* (Université des Sciences et Technologies de Lille, 2010).

[15]Laurent T., "Theoretical and experimental investigation of a new a GaN based solid state terahertz MASER", *Tesis Doctoral* (Université Montpellier 2, 2010).

[16]Faist J., Capasso F., Sivco D. L., Sirtori C., Hutchinson A. L. and Cho A. Y., "Quantum Cascade Laser", *Science* **264**, 553 (1994).

[17]Varani L, Palermo C., Millithaler J. F., Vaissière J. C., Starikov E., Shiktorov P., Gružinskis V., Mateos J., Pérez S., Pardo D. and González T., "Numerical modeling of TeraHertz electronic devices", *J. Comput. Electron.* **5**, 71 (2006).

[18]Keyes R. W., "Logevidad del transistor", *Investigación y Ciencia* **392**, 41 (2009).

[19]Fert A., "Nobel lecture: Origin, development, and future of spintronics", *Rev. Mod. Phys.* **80**, 1517 (2008).

[20]Goldhaber-Gordon D., Montemerlo M. S., Love J. C., Opiteck G. J. and Ellenbogen J. C., "Overview of Nanoelectronics Devices", *Proceedings of the IEEE* **85**, 521 (1997).

[21]Kustov V. L., Ryzhiĭ V. I. and Sigov Yu. S.,"Nonlinear plasma instabilities in semiconductors subjected to strong electric fields in the case of inelastic scattering of electrons by optical phonons", *Sov. Phys. JETP* **52**, 1207 (1980).

[22]Ryzhiĭ V. I., Bannov N. A. and Fedirko V. A., *Fiz. Tekh. Poluprovodn.* **18**, 769 (1984).

[23]Starikov E., Shiktorov P., Gružinskis V., Varani L., Palermo C., Millithaler J-F. and Reggiani L., "Terahertz generation in nitrides due to transit-time resonance assisted by optical phonon emission", *J. Phys.: Condens. Matter* **20**, 384209 (2008).

[24]Gunn J. B., "Microwave oscillations of current in III-V semiconductors", *Solid State Commun.* **1**, 88 (1963).

[25]Alekseev E. and Pavlidis D., "Large-signal microwave performance of GaN-based NDR diode oscillators", *Solid-State Electron.* **44**, 941 (2000).

[26]Sevik C. and Bulutay C., "Simulation of Millimeter-Wave Gunn Oscillations in Gallium Nitride", *Turk. J. Phys.* **28**, 369 (2004).

[27]Song A. M., Missous M., Omling P., Peaker A. R., Samuelson L. and Seifert W., "Unidirectional electron flow in a nanometer-scale semiconductor channel: A self-switching device", *Appl. Phys. Lett.* **83**, 1881 (2003).

[28]Hao Y., Yang L. A. and Zhang J. C., "GaN-based Semiconductor Devices for Terahertz Technology", *Terahertz Science and Technology* **1**, 51 (2008).

[29]Starikov E., Shiktorov P., Gružinskis V., Reggiani L., Varani L., Vaissière J. C. and Zhao J. H., "Monte Carlo simulation of the generation of terahertz radiation in GaN", *J. Appl. Phys.* **89**, 1161 (2001).

[30]Jacoboni C. and Lugli P., *The Monte Carlo Method for Semiconductor Device Simulation* (Springer-Verlag, Wien-New York, 1989).

[31]Tomizawa K., *Numerical Simulation of Submicron Semiconductor Devices* (Artech House, Boston-London, 1993).

[32]Moglestue C., *Monte Carlo simulation of semiconductor devices* (Chapman & Hall, London-New York, 1993).

[33]González T., "Análisis del ruido electrónico en materiales y dispositivos semiconductores unipolares mediante el método de Monte Carlo", Tesis Doctoral (Universidad de Salamanca, 1994).

[34]Martín M. J., "Análisis del transporte de carga y de los fenómenos del ruido electrónico en estructuras $Si/Si_{1-x}Ge_x$ bipolares", Tesis Doctoral (Universidad de Salamanca, 1996).

[35]Mateos J., "Modelización microscópica del ruido electrónico en estructuras MESFET y HEMT submicrométricas. Análisis numérico y experimental.", Tesis Doctoral (Universidad de Salamanca, 1997).

[36]Rengel R., "Análisis de los fenómenos de transporte y ruido electrónico en transistores MOSFET y SOI submicrométricos", *Tesis Doctoral* (Universidad de Salamanca, 2002).

[37]Vasallo B. G. "Transporte electrónico en estructuras de heterounión InAlAs/InGaAs: HEMTs y dispositivos balísticos de dimensiones nanométricas", *Tesis Doctoral* (Universidad de Salamanca, 2005).

[38]Iñiguez-de-la-Torre I. "Análisis de Efectos de Carga Superficial en Nanodispositivos Semiconductores Modelizados Mediante Simulaciones Monte Carlo", *Tesis Doctoral* (Universidad de Salamanca, 2008).

[39]Rodilla H. "Estudio de HEMTs basados en semiconductores de gap estrecho. Desde los materiales al dispositivo", *Tesis Doctoral* (Universidad de Salamanca, 2010).

[40]Metropolis N., "The beginning of the Monte Carlo method", *Los Alamos Science* **15**, 125 (1987).

[41]Eckhardt R., "Stan Ulam, John von Neumann, and the Monte Carlo method", *Los Alamos Science* **15**, 131 (1987).

[42]Warnock T., "Random-number generators", *Los Alamos Science* **15**, 137 (1987).

[43]Kurosawa T., Proceedings of the International Conference on the Physics of Semiconductors (Kyoto), *J. Phys. Soc. Japan* Suppl. A **49**, 345 (1966).

[44]Kurosawa T., "Monte Carlo calculation of hot electron problems", *J. Phys. Soc. Japan* Suppl. **21**, 424 (1966).

[45]Snowden C. M., *Introduction to semiconductor device modelling* (World Scientific, Singapore, 1986).

[46]Constant E., "Modelling of sub–micron devices", in *Solid State Devices*, edited by J.E. Carrol, *IOP Conf. Series* **57**, 141 (1980).

[47]González T. and Pardo D., "Physical models of ohmic contact for Monte Carlo device simulation", *Solid-State Electron.* **39**, 555 (1996).

[48]Press W. H., Flannery B. P., Teukolski S. A. and Vetterling W. T., *Numerical recipes. The art of scientific computing* (Cambridge University Press, New York, 1989).

[49]Matulionis A., Požela J. and Reklaitis A., "Monte Carlo treatment of electron-electron collisions", *Solid State Com.* **16,** 1133 (1975).

[50]Mansour N. S., Diff K. and Brennan K. F., "Ensemble Monte Carlo study of electron transport in degenerate bulk GaAs", *J. Appl. Phys.* **70**, 6854 (1991).

[51]Ashcroft N. W. and Mermin N. D., *Solid State Physics* (Saunders, Philadelphia, PA, 1976).

[52]Nag B. R., *Electron Transport in Compound Semiconductors* (Springer-Verlag, Berlin-New York-Heidelberg, 1980).

[53]Ferry D. K. and Grondin R. O., *Physics of Submicron Devices* (Plenum Press, New York, 1991).

[54]Mateos J., González T., Pardo D., Hoel V., Happy H. and Cappy A., "Improved Monte Carlo Algorithm for the Simulation of δ-Doped AlInAs/GaInAs HEMTs", *IEEE Trans. Electron Devices* **47**, 250 (2000).

[55]Hockney R. W. and Eastwood J. W., *Computer simulation using particles* (IOP, Bristol, 1988).

[56]Tiwari S., *Compound semiconductor device physics* (Academic Press, New York, 1992).

[57]Foutz B. E., O'Leary S. K., Shur M. S. and Eastman L. F., "Transient electron transport in wurtzite GaN, InN, and AlN", *J. Appl. Phys.* **85**, 7727 (1999).

[58]Goano M., Bellotti E., Ghillino E., Ghione G. and Brennan K. F., "Band structure nonlocal pseudopotential calculation of the III-nitride wurtzite phase materials system. Part I. Binary compounds GaN, AlN, and InN", *J. Appl. Phys.* **88**, 6467 (2000).

[59]Madelung O., *Semiconductors: Data Handbook* (Springer, Berlin, 2004).

[60]Barker J. M., Akis R., Ferry D. K., Goodnick S. M., Thornton T. J., Koleske D. D., Wickenden A. E. and Henry R. L., “High-field transport studies of GaN”, *Physica B* **314**, 39 (2002).

[61]Barker J. M., Ferry D. K., Koleske D. D. and Shul R. J., “Bulk GaN and AlGaN/GaN heterostructure drift velocity measurements and comparison to theoretical models”, *J. Appl. Phys.* **97**, 063705 (2005).

[62]Kemerley R. T., Wallace H. B. and Yoder M. N., “Impact of Wide Bandgap Microwave Devices on DoD Systems”, *Proceedings of the IEEE* **90**, 1059 (2002).

[63]Mateos J., González T., Pardo D., Hoël V. and Cappy A., “Monte Carlo Simulator for the Design Optimization of Low-Noise HEMTs”, *IEEE Trans. Electron Devices* **47**, 1950 (2000).

[64]Mateos J., Pérez S., Pardo D. and González T., “Monte Carlo analysis of thermal effects in GaN HEMTs”, Proceedings of the 7th Spanish Conference on Electron Devices (CDE), *IEEE* Catalog **CFP09589**, 459 (2009).

[65]Mateos J., Pérez S., Cuerdo R., Muñoz E., Calle F. and González T., “Monte Carlo Simulation of GaN HEMTs: Influence of GaN p-type Doping and High Temperature of Operation”, Proceedings of the 33rd Workshop on Compound Semiconductor Devices and Integrated Circuits (WOCSDICE), 2009.

[66]Mateos J., Pérez S., Pardo D. and González T., “High Frequency Noise in GaN HEMTs”, Proceedings of the 20th International Conference on Noise and Fluctuations (ICNF), *AIP Conference Proceedings* **1129**, 237 (2009).

[67]Rodilla H., González T., Pardo D. and Mateos J., “High-mobility heterostructures based on InAs and InSb: A Monte Carlo study”, *J. Appl. Phys.* **105**, 113705 (2009).

[68]Rodilla H., González T., Moschetti G., Grahn J. and Mateos J., “Dynamic Monte Carlo study of isolated-gate InAs/AlSb HEMTs”, *Semicond. Sci. Technol.* **26**, 025004 (2011).

[69]Sadi T., Dessenne F. and Thobel J.-L., “Three-dimensional Monte Carlo study of three-terminal junctions based on InGaAs/InAlAs heterostructures”, *J. Appl. Phys.* **105**, 053707 (2009).

[70]González T., Vasallo B. G., Pardo D. and Mateos J., “Room temperature nonlinear transport in ballistic nanodevices”, *Semicond. Sci. Technol.* **19**, S125 (2004).

[71]Mateos J., Vasallo B. G., Pardo D., González T., Pichonat E., Galloo J. -S., Bollaert S., Roelens Y. and Cappy A., “Nonlinear Effects in T-Branch Junctions”, *IEEE Electron Device Lett.* **25**, 235 (2004).

[72]Iñiguez-de-la-Torre I., Mateos J., González T., Pardo D., Galloo J. S., Bollaert S., Roelens Y. and Cappy A., “Influence of the surface charge on the operation of ballistic T-branch junctions: a self-consistent model for Monte Carlo simulations”, *Semicond. Sci. Technol.* **22**, 663 (2007).

[73]Iñiguez-de-la-Torre I., González T., Pardo D., Gardès C., Roelens Y., Bollaert S. and Mateos J., “Influence of the branches width on the nonlinear output characteristics of InAlAs/InGaAs-based three-terminal junction”, *J. Appl. Phys.* **105**, 094504 (2009).

[74]Kaushal V., Iñiguez-de-la-Torre I., Irie H., Guarino G., Donaldson W. R., Ampadu P., Sobolewski R. and Margala M., “A Study of Geometry Effects on the Performance of Ballistic Deflection Transistor”, *IEEE Trans. Nanotechnol.* **9**, 723 (2010).

[75]Mateos J., Vasallo B. G., Pardo D. and González T., “Operation and high-frequency performance of nanoscale unipolar rectifying diodes”, *Appl. Phys. Lett.* **86**, 212103 (2005).

[76]Iñiguez-de-la-Torre I., González T., Rodilla H., Vasallo B. G. and Mateos J., *Monte Carlo Simulation of Room Temperature Ballistic Nanodevices, Applications of Monte Carlo Method in Science and Engineering* (Ed. Mordechai S., InTech, 2011).

[77]Ramo S., “Currents induced by electron motion”, *Proc. IRE* **27**, 584 (1939).

[78]Shockley W., “Currents to conductors induced by a moving point charge”, *J. Appl. Phys.* **9**, 635 (1938).

[79]De Visschere P., "The validity of Ramo's theorem", *Solid-State Electron.* **33**, 455 (1990).

[80]Kim H., Min H. S., Tang T. W. and Park Y. J., "An extended proof of the Ramo-Shockley theorem", *Solid-State Electron.* **34**, 1251 (1991).

[81]Babiker S., Asenov A., Cameron N., Beaumont S. P. and Barker J. R., "Complete Monte Carlo RF Analysis of "Real" Short-Channel Compound FET's", *IEEE Trans. Electron Devices* **45**, 1644 (1998).

[82]Yoder P. D., Gärtner K. and Fichtner W., "A generalized Ramo-Shockley theorem for classical to quantum transport at arbitrary frequencies", *J. Appl. Phys.* **79**, 1951 (1996).

[83]Yoder P. D., Gärtner K., Krumbein U. and Fichtner W., "Optimized Terminal Current Calculation for Monte Carlo Device Simulation", *IEEE Trans. Computer-Aided Design* **16**, 1082 (1997).

[84]Jefimenko O. D., *Electricity and Magnetism* (Appleton-Century-Crofts, New York, 1966).

[85]Shannon C. E., "Communication in the presence of noise", *Proc. IRE* **37**, 10, (1949). Reprint as Classic Paper in: *Proc. IEEE* **86**, 447 (1998).

[86]Sevik C. and Bulutay C., "Gunn Oscillations in GaN channels", *Semicond. Sci. Technol.* **19**, S188 (2004).

[87]Sevik C. and Bulutay C., "Efficiency and harmonic enhacement trends in GaN-based Gunn diodes: Ensemble Monte Carlo analysis", *Appl. Phys. Lett.* **85**, 3908 (2004).

[88]Macpherson R. F. and Dunn G. M., "The use of doping spikes in GaN Gunn diodes", *Appl. Phys. Lett.* **93**, 062103 (2008).

[89]Starikov E., Shiktorov P., Gružinskis V., Reggiani L., Varani L., Vaissière J. C. and Zhao J. H., "Monte Carlo Simulation of THz Maser Based on Optical Phonon Transit Time Resonance in GaN", *IEEE Trans. Electron Devices* **48**, 438 (2001).

[90]Starikov E., Shiktorov P., Gružinskis V., Reggiani L., Varani L. and Vaissière J. C., "Terahertz Generation from Dynamic Free-Carrier Superlattice in n^+nn^+ InN Structures", *J. Comput Electron.* **2**, 465 (2003).

[91]Gružinskis V., Shiktorov P., Starikov E., Reggiani L., Varani L. and Vaissière J. C., "Free-carrier grating and terahertz generation from InN n^+nn^+ structures under streaming plasma instability", *Semicond. Sci. Technol.* **19**, S173 (2004).

[92]Gružinskis V., Starikov E. and Shiktorov P., "Small and Large Signal Analysis of Terahertz Generation from InN n^+nn^+ Structures with Free-Carrier Grating", *Acta Phys. Polon. A* **107**, 163 (2005).

[93]Gružinskis V., Starikov E. and Shiktorov P., "Free-carrier grating due to the optical phonon emission in InP n^+nn^+ structures", *J. Comput. Electron.* **6**, 11 (2007).

[94]Gružinskis V., Shiktorov P. and Starikov E., "Plasma Instability Noise in InP n^+nn^+ Structures: Monte Carlo simulation", *Acta Phys. Polon. A* **113**, 947 (2008).

[95]Starikov E., Shiktorov P., Gružinskis V., Varani L., Palermo C., Sabatini G., Marinchio H., Laurent T. and Reggiani L., "Anomalous behavior of electronic noise related to the onset of current instabilities in n^+nn^+ diodes", *J. Stat. Mech.* P01035 (2009).

[96]Gružinskis V., Shiktorov P. and Starikov E., "Analysis of Conditions for Free-Carrier Grating Formation in InP n^+nn^+ Structures using Monte Carlo Technique", *Acta Phys. Polon. A* **103**, 943 (2008).

[97]Katayama Y. and Komatsubara K. F., "Oscillatory Tunnel Conductance Induced by Longitudinal Optic Phonons in InSb-Oxide-Metal Structure", *Phys. Rev. Lett.* **19**, 1421 (1967).

[98]Hickmott T. W., Solomon P. M., Fang F. F., Stern F., Fischer R. and Morkoç H., "Sequential Single-Phonon Emission in GaAs-$Al_xGa_{1-x}As$ Tunnel Junctions", *Phys. Rev. Lett.* **52**, 2053 (1984).

[99]Lu P.-F., Tsui D. C. and Cox H. M., "Optical-Phonon Emission in Ballistic Transport through Microchannels of InGaAs", *Phys. Rev. Lett.* **54**, 1563 (1985).

[100]Lu P.-F., Tsui D. C. and Cox H. M., “LO-phonon oscillations and electron freeze-out in transport through In-InP and Sn-InP contacts”, *Phys. Rev. B* **35**, 9659 (1987).

[101]Vorob’ev L. E., Danilov S. N., Tulupenko V. N. and Firsov D. A., “Generation of Millimeter Radiation Due to Electric-Field-Induced Electron-Transit-Time Resonance in Indium Phosphide”, *JETP Lett.* **73**, 219 (2001).

[102]Íñiguez-de-la-Torre A., Mateos J. and González T., “Terahertz current oscillations assisted by optical phonon emission in GaN n^+nn^+ diodes: Monte Carlo simulations”, *J. Appl. Phys.* **107**, 053707 (2010).

[103]Brennan K. and Hess K., “High field transport in GaAs, InP and InAs”, *Solid-State Electron.* **27**, 347 (1984).

[104]Dendy R. O., *Plasma Dynamics* (Oxford University Press, New York, 1990).

[105]Jackson J. D., *Electrodinámica Clásica* (Ed. Alhambra, Madrid, 1980).

[106]Balocco C., Song A. M., Åberg M., Forchel A., González T., Mateos J., Maximov I., Missous M., Rezazadeh A. A., Saijets J., Samuelson L., Wallin D., Williams K., Worschech L. and Xu H. Q., “Microwave Detection at 110 GHz by Nanowires with Broken Symmetry”, *Nano Lett.* **5**, 1423 (2005).

[107]Balocco C., Kasjoo S. R., Xiaofeng F. Lu, Zhang L. Q., Alimi Y., Winnerl S. and Song A. M., “Room-temperature operation of a unipolar nanodiode at terahertz frequencies”, *Appl. Phys. Lett.* **98**, 223501, (2011).

[108]Balocco C., Halsall M., Vinh N. Q. and Song A. M., “THz operation of asymmetric-nanochannel devices”, *J. Phys.: Condens. Matter* **20**, 384203 (2008).

[109]Xu K. Y., Lu X. F., Wang G. and Song A. M. “Strong Spatial Dependence of Electron Velocity, Density, and Intervalley Scattering in an Asymmetric Nanodevice in the Nonlinear Transport Regime”, *IEEE Trans. Nanotechnol.* **4**, 451 (2008).

[110]Iñiguez-de-la-Torre I., Mateos J., Pardo D., Song A. M. and González T., “Noise and terahertz rectification linked by geometry in planar asymmetric nanodiodes” *Appl. Phys. Lett.* **94**, 093512 (2009).

[111]Xu K. Y., Lu X. F., Song A. M. and Wang G. "Enhanced terahertz detection by localized surface plasma oscillations in a nanoscale unipolar diode", *J. Appl. Phys.* **103**, 113708 (2008).

[112]Iñiguez-de-la-Torre I., Mateos J., Pardo D. and González T., "Monte Carlo analysis of noise spectra in self-switching nanodiodes", *J. Appl. Phys.* **103**, 024502 (2008).

[113]Xu K. Y., Lu X. F., Song A. M. and Wang G., "Terahertz harmonic generation using a planar nanoscale unipolar diode at zero bias", *Appl. Phys. Lett.* **92**, 163503 (2008).

[114]Iñiguez-de-la-Torre I., Mateos J., Pardo D., Song A. M. and González T.,, "Enhanced Terahertz detection in self-switching diodes", *Int. J. Numer. Model.: Electron. Netw., Devices and Fields* **23**, 301 (2009).

[115]Iñiguez-de-la-Torre I., Rodilla H., Mateos J., Pardo D., Song A. M. and González T., "Terahertz tuneable detection in self-switching diodes based on high mobility semiconductors: InGaAs, InAs and InSb", *J. Phys.: Conf. Series* **193**, 012082 (2009).

[116]Balocco C., Kasjoo S. R., Zhang L. Q., Alimi Y. and Song A. M., "Low-frequency noise of unipolar nanorectifiers", *Appl. Phys. Lett.* **99**, 113511 (2011).

[117]Åberg M., Saijets J., Song A. M. and Prunnila M, "Simulation and Modeling of Self-switching Devices", *Physica Scripta* **T114**, 123 (2004).

[118]Farhi G., Saracco E., Beerens J., Morris D., Charlebois S. A. and Raskin J.-P., "Electrical characteristics and simulations of self-switching-diodes in SOI technology", *Solid-State Electron.* **51**, 1245 (2007).

[119]Farhi G., Morris D., Charlebois S. A. and Raskin J.-P., "The impact of etched trenches geometry and dielectric material on the electrical behaviour of silicon-on-insulator self-switching diodes", *Nanotechnology* **22**, 435203 (2011).

[120]Kettle J., Whitelegg S., Song A. M., Madec M. B., Yeates S., Turner M. L., Kotacka L. and Kolarik V., "Fabrication of poly(3-hexylthiophene) self-switching diodes using thermal nanoimprint lithography and argon milling", *J. Vac. Sci. Technolog. B* **27**, 2801 (2009).

[121]Irshaid Mustafa Y., Balocco C., Luo Y., Bao P., Brox-Nilsen C. and Song A. M., "Zinc-oxide-based planar nanodiodes operating at 50 MHz", *Appl. Phys. Lett.* **99**, 092101 (2011).

[122]Xu K. Y., Wang G. and Song A. M., "Gunn oscillations in a self-switching nanodiode", *Appl. Phys. Lett.* **93**, 233506 (2008).

[123]González T., Iñiguez-de-la-Torre I, Pardo D., Mateos J. and Song A. M. "Gunn Oscillations in Asymmetric Nanodiodes Based on Narrow and Wide Band-Gap Semiconductors: Monte Carlo Simulations", *Proceedings* of the 33rd Workshop on Compound Semiconductor Devices and Integrated Circuits (WOCSDICE), 2009.

[124]González T., Iñiguez-de-la-Torre I., Pardo D., Mateos J. and Song A. M., "Monte Carlo analysis of Gunn oscillations in narrow and wide band-gap asymmetric nanodiodes", *J. Phys.: Conf. Series* **193**, 012018 (2009).

[125]González T., Iñiguez-de-la-Torre I., Pardo D, Song A. M. and Mateos J., "THz Generation Based on Gunn Oscillations in GaN Planar Asymmetric Nanodiodes", 22nd International Conference on Indium Phosphide and Related Materials (IPRM), *IEEE*, (2010).

[126]Íñiguez-de-la-Torre A., Íñiguez-de-la-Torre I., Mateos J., González T., Sangaré P., Faucher M., Grimbert B., Brandli V., Ducournau G. and Gaquière C., "Searching for THz Gunn oscillations in GaN planar nanodiodes", *J. Appl. Phys.* **111**, 113705 (2012).

[127]Yilmazoglu O., Mutamba K., Pavlidis D. and Karaduman T., "First Observation of Bias Oscillations in GaN Gunn Diodes on GaN Substrate", *IEEE Trans. Electron Devices* **55**, 1563 (2008).

[128]Ridley B. K. and Watkins T. B., "The Possibility of Negative Resistance Effects in Semiconductors", *Proc. Phys. Soc.* **78**, 293 (1961).

[129]Hilsum C., "Transferred Electron Amplifiers and Oscillators", *Proceedings of the IRE* **50**, 185 (1962).

[130]Ridley B. K., "Specific Negative Resistance in Solids", *Proc. Phys. Soc.* **82**, 954 (1963).

[131]Kroemer H., "Theory of the Gunn effect", *Proceedings of the IEEE* (Correspondence) **52**, 1736 (1964).

[132]Butcher P. N., Fawcett W. and Hilsum C., "A simple analysis of stable domain propagation in the Gunn effect", *Brit. J. Appl. Phys.* **17**, 841 (1966).

[133]Butcher P. N., "The Gunn effect", *Rep. Prog. Phys.* **30**, 97 (1967).

[134]Kurokawa K., "Some Basic Characteristics of Broadband Negative Resistance Oscillator Circuits", *The Bell System Technical Journal* **48**, 1937 (1969).

[135]Torrens A. B., "Negative differential conductivity effects in semiconductors", *Tesis Doctoral* (University of British Columbia, 1969).

[136]Brophy J. J., *Basic electronics for scientists* (McGraw-Hill, New York, 1972).

[137]Sze S. M. and K. K. Ng, *Physics of Semiconductor Devices* (Ed. Wiley-Interscience, New Jersey, 2007).

[138]Solymar L. and Walsh D., *Electrical Properties of Materials* (Oxford University Press, New York, 2010).

[139]Yu P. Y. and Cardona M., *Fundamentals of Semiconductors: Physics and Materials Properties* (Springer-Verlag, Berlin-Heidelberg, 2010).

[140]Sangaré P., Ducournau G., Grimbert B., Brandli V., Faucher M., Gaquière C., Íñiguez-de-la-Torre A., Íñiguez-de-la-Torre I., Millithaler J. F., Mateos J. and González T., "Experimental Demonstration of Direct Terahertz Detection at Room-Temperature in AlGaN/GaN Asymmetric Nanochannels". *Nano Lett.* Manuscript submitted for publication (2012).

[141]Starikov E., Shiktorov P., Gružinskis V., Reggiani L., Varani L. and Vaissière J. C., "Noise Enhancement as Indicator of Instability Onset in Semiconductor Structures", Proceedings of the 18th International Conference on Noise and Fluctuations (ICNF), *AIP Conference Proceedings* **780**, 791 (2005).

[142]Shiktorov P., Starikov E., Gružinskis V., Varani L. and Reggiani L., "Giant enhancement of low-frequency noise as precursor for the onset of a high-frequency instability", Proceedings of the 20th International Conference on Noise and Fluctuations (ICNF), *AIP Conference Proceedings* **1129**, 179 (2009).

[143]Íñiguez-de-la-Torre A., Íñiguez-de-la-Torre I, Mateos J. and González T., "Correlation between low-frequency current-noise enhancement and high-frequency oscillations in GaN-based planar nanodiodes: A Monte Carlo study", *Appl. Phys. Lett.* **99**, 062109 (2011).

VNIVERSITAS
STVDII
SALAMANTINI